ACS OMEGA

Article

Cite This: ACS Omega 2017, 2, 9040−9056

# CdS QDs-Decorated Self-Doped γ-$Bi_2MoO_6$: A Sustainable and Versatile Photocatalyst toward Photoreduction of Cr(VI) and Degradation of Phenol

Debasmita Kandi,[†] Satyabadi Martha,*[,†] Arun Thirumurugan,[‡] and K. M. Parida*[,†]

[†]Centre for Nano Science and Nano Technology, Institute of Technical Education and Research, Siksha 'O' Anusandhan University, Bhubaneswar 751030, India

[‡]Advanced Material Laboratory, Department of Mechanical Engineering, University of Chile, Santiago 8370448, Chile

Supporting Information

**ABSTRACT:** In this work, CdS quantum dots (QDs)-sensitized self-doped $Bi_2MoO_6$ has been synthesized using glucose as reducing agent by hydrothermal method, followed by in situ deposition of the QDs. The synthesized catalyst has been employed to reduce toxic Cr(VI) and degrade phenol from the aqueous solution. The structural, optical, and electrochemical characterizations are performed using X-ray diffraction, UV−vis diffuse reflection, photoluminescence (PL), scanning electron microscopy, transmission electron microscopy (TEM), Fourier transform infrared spectroscopy, and electrochemical impedance spectroscopy. The optical properties were precisely investigated by calculating the Urbach energy, PL, and photoluminescence excitation spectra. The orderly distribution of QDs is confirmed from the correlation between full width at half-maximum of PL spectra, Urbach energy, and TEM analysis. The versatile photocatalytic activity has been tested toward Cr(VI) reduction and degradation of phenol. 3% CdS QDs-sensitized self-doped $Bi_2MoO_6$ showed highest activity, i.e., 97 and 47.5% toward reduction of Cr(VI) and degradation of phenol under solar light. The reduction of Cr(VI) by the catalyst is supported by the kinetics and determination of the $pH_{PZC}$ value. In addition to this, the photostability and reusability test showed that the catalyst can be reused up to five cycles without diminishing its activity.

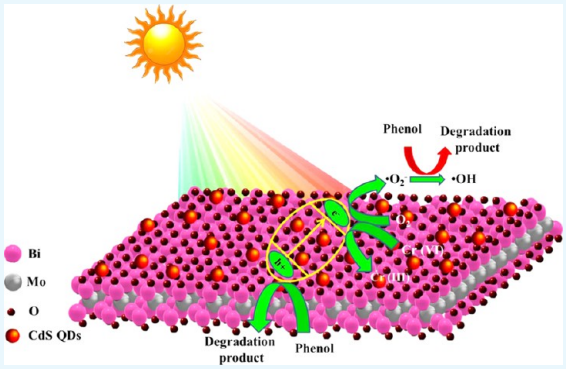


## 1. INTRODUCTION

$Bi_2MoO_6$ is an active and simplest member of the Aurivillius oxide family of layered perovskites that has attracted increasing attention in the field of photocatalysis because of its luminescence, photocatalytic properties, low band gap energy, layered structure, and suitable band edge potential.[1−3] Additionally, its resistivity toward corrosion, mesoporosity, low cost, outstanding chemical stability, and attractive physicochemical properties also contribute to its improved photocatalytic activity. The Aurivillius oxide (γ-$Bi_2MoO_6$) possesses a distinctive layered structure with perovskite wedges of $MoO_6$ octahedra sandwiched between alternating $(Bi_2O_2)^{2+}$ layers.[4] It should be mentioned here that depending on the proportions of bismuth and molybdenum present bismuth molybdate (BMO) may exist in a variety of phases, among which the $Bi_2Mo_3O_{12}$ or α-phase,[5] the $Bi_2Mo_2O_9$ or β-phase,[6] and the $Bi_2MoO_6$ or γ-phase are commonly studied.[7] The ratio of Bi to Mo in α-, β-, and γ-phases are 2/3, 2/2, and 2/1, respectively. Of these phases, γ-phase is known to possess more mobile oxygen, whereas α- and β-phases provide more absorption sites for hydrocarbons. However, the consensus is that mixture of both γ-phase and α- or β-phase shows better photocatalytic activity than any single phase of bismuth molybdate due to the synergy effect[8] that takes place in the mixture. This modification of the individual γ-phase is performed to optimize its photocatalytic activity, viz., to overcome its inherent bottlenecks, which include low efficiency toward utilization of visible light, fast recombination and transport of photogenerated charge carriers, modest surface area, less active sites, and poor selectivity toward redox reactions. Apart from the synergic mixture of interphase composites, the photocatalytic activity has also been improved by making composite with noble metal (Ag, Pt). Yuan et al.[9] decorated a $Bi_2MoO_6$ microsphere uniformly with Ag nanoparticles for the photodegradation of methyl orange, methylene blue, and rhodamine B. Ag here acts as electron sink, which facilitates charge transfer via the Schottky barrier at the interface of the noble metal and $Bi_2MoO_6$. Zhang and co-workers[10] synthesized ultrathin $Bi_2MoO_6$ nanoplates loaded with Pt nanoparticles as co-catalyst and demonstrated their superior photocatalytic performance toward aerobic selective oxidation of benzyl alcohol. Understanding the significance of surface plasmon resonance (SPR)

Received: August 25, 2017
Accepted: December 1, 2017
Published: December 18, 2017




DOI: 10.1021/acsomega.7b01250
ACS Omega 2017, 2, 9040−9056

and sidestepping the high cost of noble metals, Zhao et al.[11] synthesized Bi co-catalyst loaded on $Bi_2MoO_6$ microspheres nanohybrid inspiring by the fact that Bi also exhibits the noble metal behavior, i.e., direct plasmonic resonance and the matched band edge positions with $Bi_2MoO_6$.

To improve the visible light absorption ability, the effective separation of the electron−hole pairs, and the photocatalytic activity of Bi/$Bi_2MoO_6$, in this work, CdS quantum dots (QDs) have been incorporated into the reaction system to activate the substrate and effectively lower the activation energy of the desired reaction because of their quantum confinement effect, high dispersity, large absorption coefficient, ultrasmall particle size, narrow band gap of around 2.29 eV, and the wavelength- and size-dependent photoluminescence (PL) emission.[12]

In this work, we have designed solar light-driven CdS QDs-sensitized self-doped $Bi_2MoO_6$ for the reduction of Cr(VI) and degradation of phenol. Detailed investigation of the prepared materials like phase purity, crystal structure, optical and photoluminescence properties, and effect of point of zero charge (PZC) was carried out. The prepared material exhibit the synergistic effect of Bi and CdS QDs for better photocatalytic activity toward fast reduction of Cr(VI) and phenol degradation. The mechanisms of both Cr(VI) and degradation of phenol have been studied in detail. The mechanistic pathway is well explained by employing the scavenger test and the involvement of active species, which is established from the respective confirmatory tests.

## 2. EXPERIMENTAL SECTION

**2.1. Synthesis of Bismuth Molybdate (BMO) and Self-Doped Bismuth Molybdate (BBMO).** For the synthesis of BMO, the typical procedure involves the dissolution of 0.242 g of $Bi(NO_3)_3·5H_2O$ and 0.06 g of $Na_2MoO_4·2H_2O$ in 10 mL of ethylene glycol separately. The two solutions were mixed and dropwise added to 30 mL of isopropanol, followed by stirring for 20 min. Then, the prepared solution was transferred to a stainless steel autoclave and heated at 160 °C for 24 h, followed by cooling to room temperature. The BMO sample was collected by centrifugation and washed several times with water and once with ethanol and finally dried at 80 °C for few hours.[13]

To synthesize BBMO, 5 mL of ethylene glycol (EG; Merck) containing 1.6866 g of $Bi(NO_3)_3·5H_2O$ (Merck) marked as solution A and 5 mL of EG containing 0.4210 g of $Na_2MoO_4·2H_2O$ marked as solution B were prepared. Solution B was then added dropwise to solution A with continuous stirring. To this mixture, 20 mL of EG was added and stirred to get a clear solution. A small amount of glucose (0.616 g; Merck) was added to get suspension with strong stirring. Then, the solution was transferred to a 100 mL stainless steel Teflon-lined autoclave and heated at 160 °C for 20 h. After the hydrothermal treatment, the product was collected by centrifugation and subsequent washing with water and ethanol two times each. The deep gray Bi/$Bi_2MoO_6$ was dried overnight at 60 °C and symbolized as BBMO.[11]

**2.2. Synthesis of CdS QDs-Sensitized BBMO.** To prepare CdS QDs-sensitized Bi/$Bi_2MoO_6$ (CBBMO), particular amount of BBMO was taken and the procedure to deposit required weight percentage of CdS QDs was followed according to our previous work.[12] Briefly, appropriate amount of BBMO was added to a 75 mM $Cd(NO_3)_2·2H_2O$ solution. Requisite amount of thioglycolic acid (TGA) was added to the solution so that the mole ratio of 1:2 was maintained between TGA and CdS QDs, and the pH of the solution was adjusted to 10.5 with 1 M NaOH. After this, $Na_2S$ was added and the prepared solution was stirred at 65 °C for 30 min. Then, after 90 min aging, the prepared sample was collected by centrifugation, followed by three times washing with water and once with ethanol. Finally, the composite was dried in a vacuum desiccator.

**2.3. Experimental Protocol for Reduction of Cr(VI) and Phenol Degradation.** For the reduction of Cr(VI), the aqueous solution of $K_2Cr_2O_7$ was used. A 20 mL volume of 100 ppm hexavalent Cr solution was taken with 0.02 g of catalysts to test the photocatalytic activity. To check the effect of pH on the photocatalytic reduction process, the pH of the solution was maintained at 2, 4, 6, and 8. Then, the suspension was stirred under dark condition for 30 min to attain the adsorption and desorption equilibrium before irradiation under solar light (100 000 lx). At different time intervals, the catalysts were separated by centrifugation and the supernatant was used for colorimetric analysis at 540 nm by 1,5-diphenylcarbazide (DPC) method using a JASCO V-750 UV−Vis spectrophotometer.[14] Additionally, the remained Cr in the sample after the experiment was also determined.[15]

Photocatalytic degradation of phenol was carried out by taking 20 mg of catalyst with 20 mL of 10 ppm phenol. Then, the suspension was stirred under dark condition for 30 min to attain the adsorption and desorption equilibrium before irradiation of solar light. Then, the pH of phenol solution was maintained at 2, 4, 6, and 8. After the photocatalytic experiment, the catalyst was extracted from the phenol solution by centrifugation and the residue was directly analyzed by a JASCO V-750 UV−Vis spectrophotometer.

**2.4. Analytical Characterization.** The phase purity and crystal structure of the CdS QDs-sensitized self-doped bismuth molybdate samples were analyzed by a Rigaku Miniflex instrument using Cu K$\alpha$ radiation ($\lambda$ = 1.54 Å) in the 2$\theta$ range of 20−80°. A JASCO V-750 UV−Vis spectrophotometer was used to measure the diffuse reflection UV−vis (DRUV−vis) spectra in the wavelength range of 200−800 nm. The photoluminescence property of the prepared samples was analyzed by a JASCO-FP-8300 fluorescence spectrometer. The emission and excitation spectra were taken to explain the uniform distribution of QDs on the surface of BBMO. Scanning electron microscopy (SEM) was carried out using ZEISS SUPRA 55. The microsphere structure of BBMO and ultrasmall particle size of CdS QDs were investigated by a TEM-JEOL-2010- 200 kV instrument. The mode of molecular vibration was determined by a FT/IT-4600 Fourier transform infrared spectrometer in the range of 4000−400 $cm^{-1}$. X-ray photoelectron spectroscopy (XPS) was performed with a VG Microtech Multilab ESCA 3000 spectrometer using a non-monochromatized Mg K$\alpha$ X-ray source. The C 1s peak was used for binding energy correction, which arises from adventitious source. The electrochemical study of the prepared samples was carried out by a multichannel Ivium potentiostat to know the photoelectrochemical properties. This was carried out in a Pyrex electrochemical cell using the synthesized catalysts as the working electrode, platinum sheet as the counter electrode, and Ag/AgCl as the reference electrode. The electrolyte utilized here to analyze the study was 0.1 M $Na_2SO_4$, and a 300 W Xe lamp was used for light irradiation with a 400 nm cutoff filter.



DOI: 10.1021/acsomega.7b01250
ACS Omega 2017, 2, 9040−9056

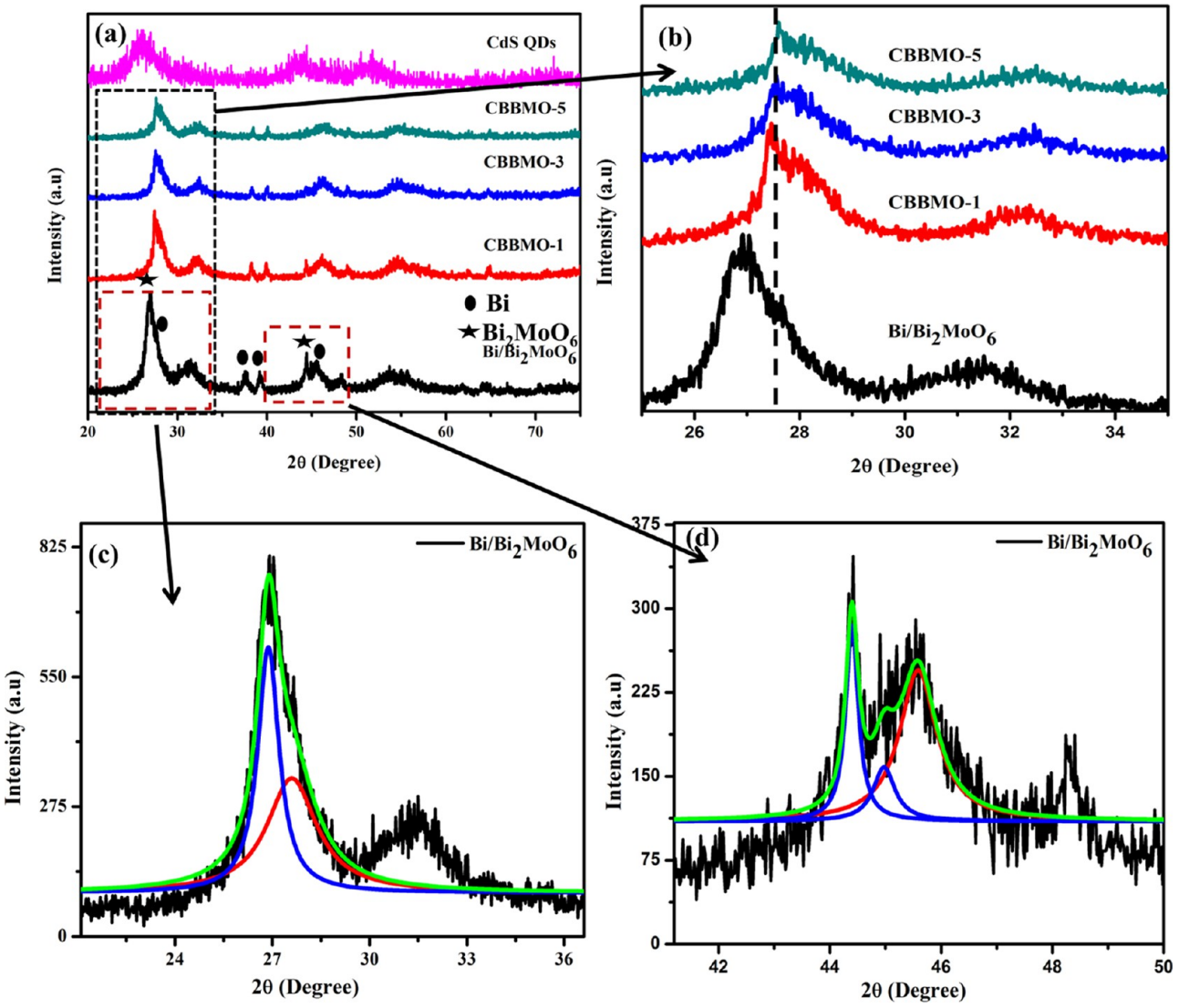


**Figure 1.** (a) XRD pattern and (b) enlarged view of pure $Bi/Bi_2MoO_6$ and the synthesized composites, $Bi/Bi_2MoO_6$/CdS QDs; (c, d) enlarged view of deconvoluted XRD pattern showing peak position of both Bi and $Bi_2MoO_6$.

## 3. RESULTS AND DISCUSSION

**3.1. Phase Structure.** Figure 1a shows the X-ray diffraction (XRD) pattern describing the crystal structure and phase purity of the as-prepared photocatalysts. The XRD pattern of $Bi/Bi_2MoO_6$ (BBMO) consists of diffraction peaks for both orthorhombic $Bi_2MoO_6$ (JCPDS no. 21-0102) and rhombohedral Bi (JCPDS no. 44-1246). Several diffraction peaks at $2\theta$ values of 27.01, 31.2, 44.2, 53.6, 53.8, and 55.7° are indexed as (131), (200), (202), (062), (133), and (191) crystal planes of $Bi_2MoO_6$. In addition to these, diffraction peaks at 27.8, 37.5, 39.2, and 45.6° are observed corresponding to the (012), (104), (110), and (006) planes in prepared composite materials, which confirms the occurrence of Bi in metallic state. The XRD result confirmed the formation of well crystalline materials without any impurities. In addition to this, no characteristic diffraction peaks of CdS QDs are observed, which is attributed to low CdS QDs content in the prepared samples.[12] As the XRD peaks of $Bi_2MoO_6$ and metallic Bi are overlapped in the range of 27−28 and 44−46°, the corresponding planes are deconvoluted as presented in Figure 1c,d. It represents the existence of metallic Bi peaks at 27.8 and 45.6° corresponding to the (012) and (006) planes. With gradual increase in the loading amount of CdS QDs in $Bi/Bi_2MoO_6$, there is shifting of peaks to higher angles owing to the synergistic interaction between CdS QDs and $Bi/Bi_2MoO_6$.[16] Additionally, the loading amount of CdS QDs could inhibit the crystal growth of $Bi/Bi_2MoO_6$, resulting in a weaker and broader peak.[17]

**3.2. Optical Studies.** The optical absorption properties of the as-prepared samples were investigated by UV−vis diffuse reflection spectroscopy (DRS) in the range of 200−800 nm. Figure 2a depicts that photoabsorption of pure BMO, BBMO, and CBBMO composites reflects in both UV and visible regions with strong light absorption between 300 and 700 nm. Its absorption range is also extended to near-IR region, which is contributed to light scattering and SPR effects of Bi metal.[11] It is also observed from Figure 2a that the absorbance spectra of BBMO and CBBMO consist of one strong and one small shoulder band in the UV region. The small shoulder band around 220−330 nm is attributed to the interband transition from valence band (consists of O 2p orbitals) to conduction band, which is made up of Mo 4d orbitals and Bi 6p orbitals.[5] In addition to this, CdS QDs have high absorbance value that shows strong absorption up to 580 nm and the steep shape is



DOI: 10.1021/acsomega.7b01250
ACS Omega 2017, 2, 9040−9056

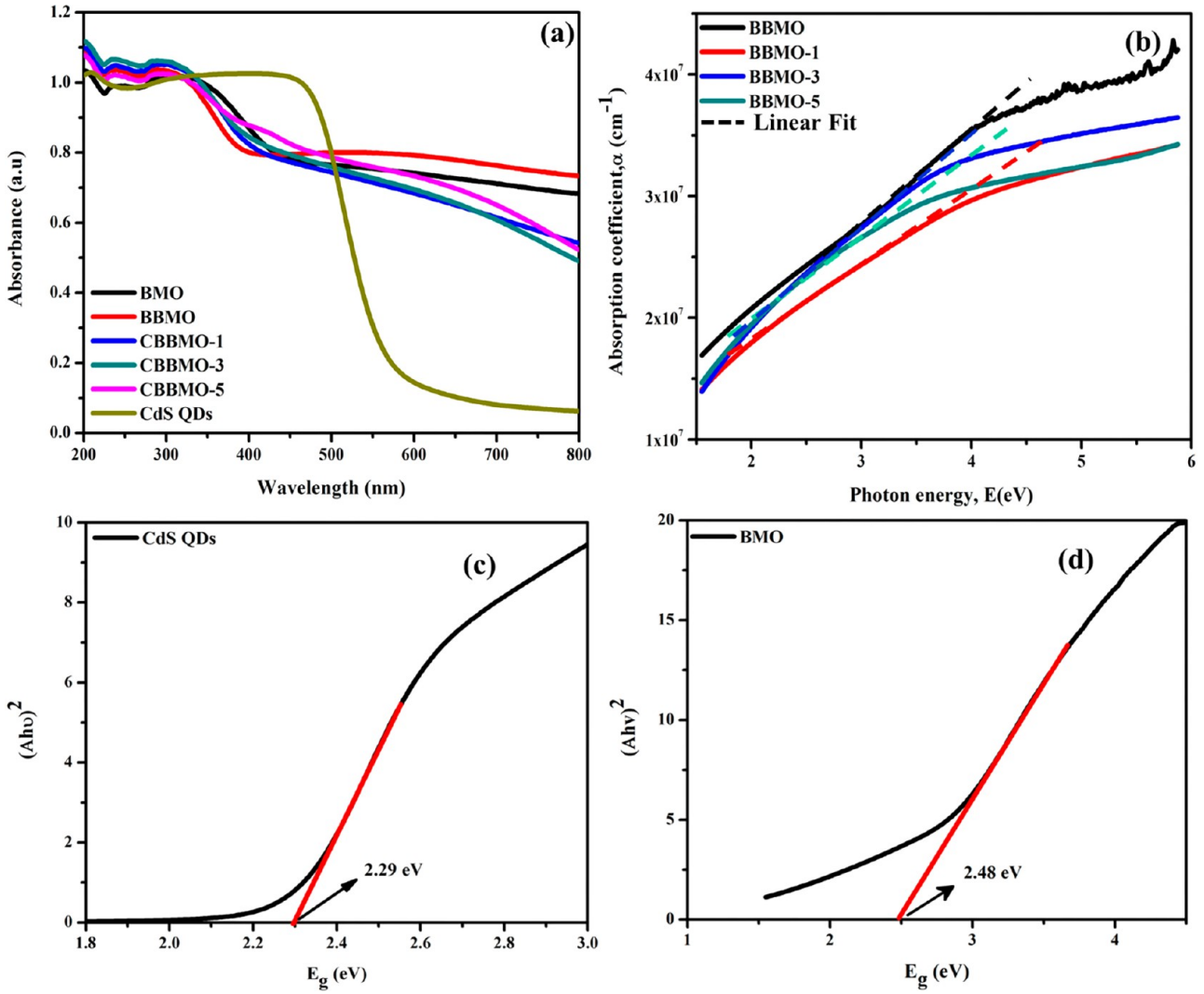


**Figure 2.** UV−vis DRS of BMO, BBMO, CdS QDs, and CBBMO composites; (b) Urbach energy of prepared samples; (c) band gap of CdS QDs; and (d) band gap of bismuth molybdate.

due to band gap transitions.[12] Moreover, no distinct maxima is found, rather a plateau-shaped spectrum is observed, which is attributed to different electronic structure. With increasing the loading amount of CdS QDs, the optical absorption shifted toward higher wavelength, which played a vital role in photocatalytic activity. This broad absorption band is attributed to uniform particle size distribution, and the red shift absorbance is attributed to the present localized states.[12] Also the observed red shift is consistent with the change in color of photocatalysts from deep gray to dark green. Consensus is that, on account of SPR effect, Bi-modified nanocomposites show improved light absorption, which is one of the important characteristics of enhanced photocatalytic activity. The direct band gaps of CdS QDs and BMO are calculated by the equation $\alpha h\upsilon = K(h\upsilon - E_g)^{1/2}$, where the symbols bear their usual designations values, that is, "$\alpha$" is the absorption coefficient, $h\upsilon$ is the photon energy, $K$ is a constant, and $E_g$ is the optical band gap energy. It should be mentioned here that absorption coefficient ($\alpha$) can be replaced by absorbance ($A$) because the concentration ($c$) and the optical path length ($l$) are invariable in the present situation.

**3.3. Calculation of Urbach Energy.** Urbach tail gives information about defects, disorder, band structure, and electron−phonon interaction in almost all amorphous semiconductors, degenerately doped crystalline materials, and in many ionic crystals in the weak absorption or low-energy side of the optical spectra. In Figure 2b, the absorption coefficient follows an exponential change, and this type of exponential decay is known as Urbach tail, which follows eq 1.

$$\alpha = \alpha_0 \, e\left(\frac{E}{E_U}\right) \tag{1}$$

where $\alpha_0$ is a constant, $E$ is the incident energy, and $E_U$ is the Urbach energy.

Taking natural logarithm on both sides, we have

$$\ln \alpha = \ln \alpha_0 + \frac{E}{E_U} \tag{2}$$

From eq 2, the reciprocal of the slope of this exponential graph plotted between $\ln \alpha$ and incident energy ($E$) determines the Urbach energy value ($E_U$). Additionally, $E_U$ is an expected explanation for density of states, especially in low-dimensional semiconductors in a nonvacated environment.[18−20] If the width of the exponential tail is large, there is more density of defect states in the material, which indicates fast recombination of



DOI: 10.1021/acsomega.7b01250
ACS Omega 2017, 2, 9040−9056

charge carriers.[18] So, to delay the recombination of charge carriers and improve the photocatalytic application, it is important to find a material having small Urbach energy ($E_U$). Table 1 shows the calculated Urbach energy and band gap values of all of the prepared samples. From Table 1 and Figure 2b, it is observed that CBBMO-3 has the lowest $E_U$ value among the prepared composites, which is an indication of containing less density of states and have undergone delayed recombination of photoexcited charge carriers. This characteristic property is also in well agreement with the PL behavior of CBBMO-3, which is discussed in the next section.

**Table 1. Band Gap, Full Width at Half-Maximum (FWHM), and Urbach Energy of Prepared BBMO Samples**

| catalyst | band gap (eV) | FWHM of PL peak (nm) | Urbach energy (eV) |
|---|---|---|---|
| CBBMO-1 | 2.70 | 45.83 | 3.71 |
| CBBMO-3 | 2.65 | 44.99 | 2.56 |
| CBBMO-5 | 2.51 | 45.74 | 2.80 |

**3.4. Photoluminescence Behavior.** To provide evidence about the transfer and degree of recombination of photoexcited charge carriers in semiconductors, PL spectroscopy is proved to be an effective method. As shown in Figure 3a, the prepared neat material and all of the composites show a strong emission peak at ca. 415 nm and a small peak at 468 nm. The former peak is due to defect-related luminescence (blue luminescence), and the latter is because of band gap transition. To acquire more information about the optoelectronic properties of the as-synthesized samples, photoluminescence (PL) emission and photoluminescence excitation (PLE) spectroscopy is performed in detail. In addition to this, it is very clear from Figure 3a that CBBMO-3 shows the lowest PL intensity compared to the other made composites, which is an indication of delayed recombination of excited charge carriers and better photocatalytic activity of the concerned sample. Figure 3b shows a comparison study between FWHM of PL emission peak calculated from Figure 3a and Urbach energy calculated from absorption coefficient in the previous section. It is clearly observed that both the factors follow a similar trend with

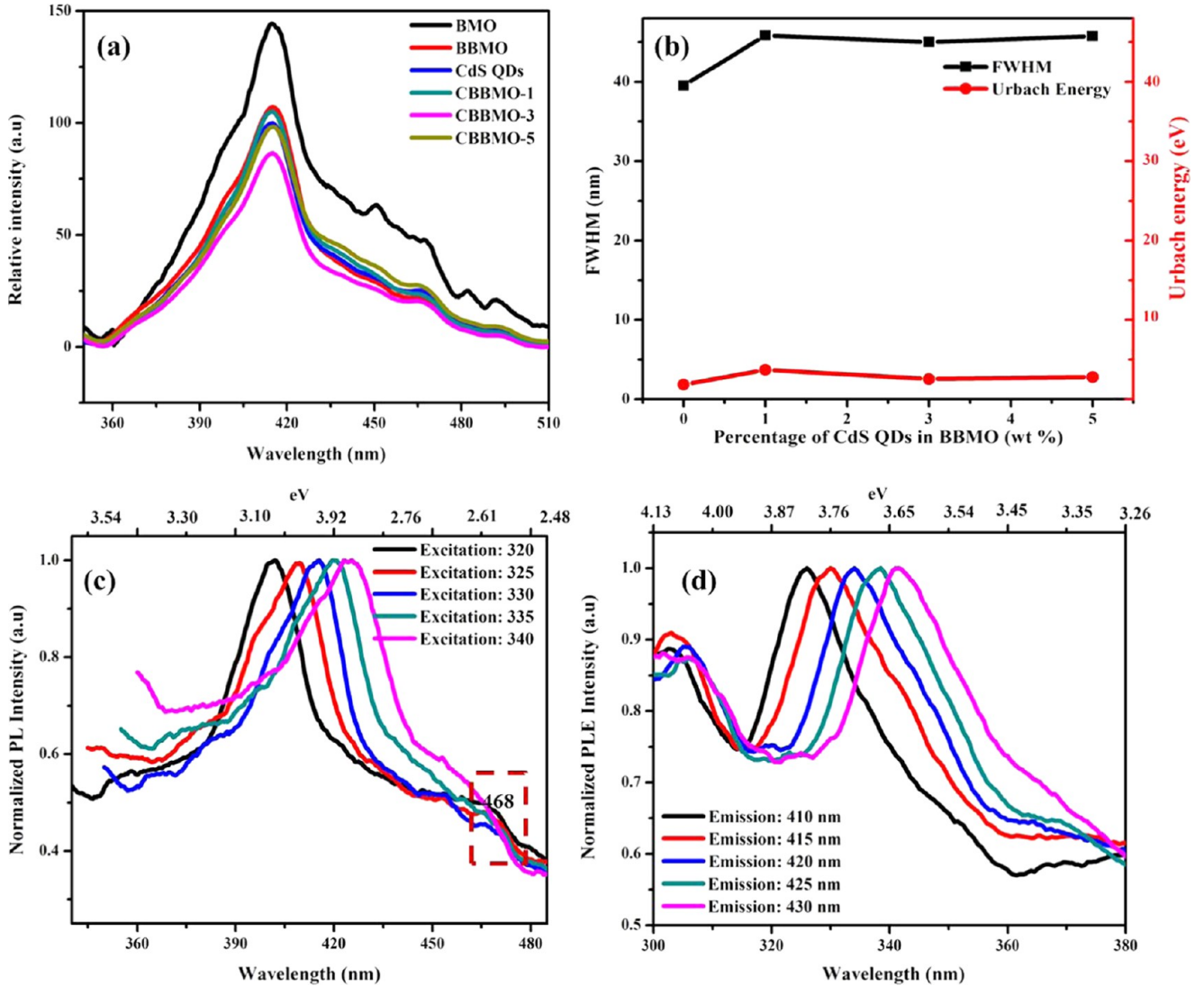


**Figure 3.** (a) Photoluminescence spectra of BMO, BBMO, CdS QDs, and the prepared composites at excitation wavelength of 330 nm; (b) comparison of change in FWHM of PL emission peak and Urbach energy; (c) normalized PL spectra of CBBMO-3 at excitation wavelengths of 320, 325, 330, 335, and 340 nm; and (d) normalized PLE spectra of CBBMO-3 at emission wavelengths of 410, 415, 420, 425, and 430 nm.



DOI: 10.1021/acsomega.7b01250
ACS Omega 2017, 2, 9040−9056

increasing loading amount of CdS QDs, which indicates that the source of foundation of both absorption and emission ascends from similar states.[21] The FWHM and $E_U$ values of the prepared composites follow the following order CBBMO-1 > CBBMO-5 > CBBMO-3. All of the values of calculated band gap, FWHM from PL peak, and Urbach energy are compiled in Table 1. It is observed from Table 1 that CBBMO-3 shows the least FWHM and Urbach energy compared to the CBBMO composites, which indicates the low disorder among these. Uniform distribution of QDs on BBMO surface is analyzed by varying different excitation wavelengths in support of wavelength-dependent PL behavior of QDs.

Figure 3c,d represents PL and PLE spectra of CBBMO-3 at different excitation and emission wavelengths, respectively. The observed data are presented in Table 2.

**Table 2. Extracted Data from Figure 3c,d[a]**

| fixed excitation | observed emission | fixed emission | observed excitation |
|---|---|---|---|
| 320 | 401.46 | 410 | 325.54 |
| 325 | 408.89 | 415 | 329.98 |
| 330 | 415.32 | 420 | 333.94 |
| 335 | 419.76 | 425 | 338.16 |
| 340 | 424.74 | 430 | 341.37 |

[a]Note: All of the given data in this table are in nanometer scale.

In Figure 3c, when the excitation wavelengths are varied in the range of 320−340 nm at an interval of 5 nm, it has been observed that the emission spectra are gradually and periodically shifted toward higher wavelength (401.46−424.74 nm). On the contrary, when emission wavelengths are varied in the range of 410−430 nm at the same interval, PLE spectra are exhibited at the wavelength nearly same as that of the fixed excitation wavelength, as mentioned in Figure 3c. From this analysis, the Stokes shift is calculated to be 84 nm (Figure S1), which indicates the weak self-absorption and low energy loss of the composites.[22] Because the broad symmetric emission peaks are not at constant wavelength when excited with various excitation wavelengths, it can be suggested that the CBBMO composites are not with a monodisperse set of CdS QDs.

**3.5. SEM.** The structure and morphology of the BBMO and all of the prepared composites were investigated by field emission scanning electron microscopy (FESEM). As shown in Figure 4a,b, the microsphere morphology of BBMO is clearly revealed with average particle size of 1.5 $\mu$m and also with some interspaced nanoparticles of the same. The interspaced nanoparticles are formed because of the reducing agent taken (glucose). During the synthesis, although the amount of glucose taken for the purpose of formation of microsphere morphology of BBMO, still it has inhibited somehow the anisotropic development of BBMO.[11] Figure 4c−h represents the distinctive SEM images of all CBBMO composites, where the deposition of CdS QDs on the surface of BBMO is clearly visible, which confirms the formation of the QDs. In Figure 4c,d (magnified image), the deposition of the QDs is less noticeable compared to other SEM images of CBBMO composites as a result of its small loading amount (1 wt %). The deposition of CdS QDs on the BBMO surface is more prominent in CBBMO-3 and CBBMO-5, as shown in Figure 4e−h. It is observed from the SEM images of all of the CBBMO composites (Figure 4c−h) that irregular spherical and apparent agglomerated QDs have partially covered the BBMO surface.

**3.6. Transmission Electron Microscopy (TEM).** The microsphere morphology of BBMO and ultrasmall particle size of the as-prepared CdS QDs are clearly visible from the high-resolution transmission electron microscopy (HRTEM) images. Figure 5a represents the TEM image and Figure 5b represents the HRTEM image of microspherical BBMO, which is in resemblance with the corresponding FESEM analysis. The $d$ spacing value mentioned in the figure corresponds to the (131) and (012) planes of $Bi_2MoO_6$ and Bi, respectively. The ultrasmall size of CdS QDs is confirmed from Figure 5c,d, which is representative of about 3.5 nm CdS QDs. The inset of Figure 5c clearly reveals the lattice spacing of CdS QDs, which corresponds to (111) crystal plane (0.33 nm). All of these obtained values of $d$ spacing are in well coincidence with the XRD analysis. The TEM image of composite CBBMO-3 is represented in Figure 5e. The coexistence of $Bi_2MoO_6$, Bi, and CdS QDs is evidenced from the HRTEM image (Figure 5f).

**3.7. Fourier Transform Infrared (FTIR) Spectroscopy.** To explore the chemical composition and mode of molecular vibration, FTIR spectra of BBMO and CBBMO catalysts were analyzed in the range of 4000−400 $cm^{-1}$, which is demonstrated in Figure 6. The peak at 448 $cm^{-1}$ is the representative peak for Bi−O stretching vibrational modes, and the band at 584 $cm^{-1}$ is the bending vibration mode of $MoO_6$ octahedron.[23] The peaks positioned at 796 and 842 $cm^{-1}$ can be correspondingly ascribed to the symmetric and asymmetric Mo−O stretching vibration modes of the corner sharing $MoO_6$ octahedron.[24] The peak retained at 2360 $cm^{-1}$ is attributed to the antisymmetrical stretching mode of carbon dioxide.[25] Peaks centered at 1620 and 3415 $cm^{-1}$ correspond to H−O−H bending and O−H stretching vibration modes of absorbed free water.[26] As the prepared QDs are capped with thioglycolic acid (TGA), the C−O stretching is observed in the range of 990−1150 and the peaks at 400−700 $cm^{-1}$ are attributed to Cd−S stretching.[27] It should be mentioned here that the S−H stretching at 2550−2970 $cm^{-1}$ is absent in TGA-capped CdS QDs, which is due to the covalent bonding between thiols and Cd atom of CdS QDs.[28] The FTIR spectra for pure TGA and TGA-capped CdS QDs are given in Figure S2.

**3.8. Chemical Composition.** The XPS analysis represents the surface chemical composition of CBBMO-3 composite. The presence of constituent elements, i.e., Bi, Mo, O, Cd, and S, is confirmed from the survey scan (Figure 7a). As shown in Figure 7b, two high-resolution and strong peaks are centered at 159.2 and 164.5 eV, which are due to $4f_{7/2}$ and $4f_{5/2}$, respectively, of $Bi^{3+}$. In addition to these two peaks, other two peaks at 156.7 and 162.4 eV are obtained, which confirms the metallic state of Bi.[11] Figure 7c reveals that peaks at 232.5 and 235. 6 eV correspond to $3d_{5/2}$ and $3d_{3/2}$ of $Mo^{6+}$ oxidation state in CBBMO-3.[29] The symmetric peak at 530.5 eV (O 1s) is attributed to Bi−O chemical bonding. Two peaks at 405.3 and 412.2 eV are ascribed to $Cd_{5/2}$ and $Cd_{3/2}$, respectively, and confirm the +2 state of Cd (Figure 7e). The presence of S at the junction is also proved from Figure 7f.[30]

**3.9. Photoelectrochemical Analysis.** Mott−Schottky (MS) analysis, linear sweep voltammetry, and electrochemical impedance spectroscopy of BBMO and CBBMO composites were investigated to conclude the high performance toward electrochemical properties. Generally, the band edge position as well as the type of semiconductor, the photocurrent response, the charge carrier separation or transport, etc. are being examined from these above-mentioned analysis.



DOI: 10.1021/acsomega.7b01250
ACS Omega 2017, 2, 9040−9056

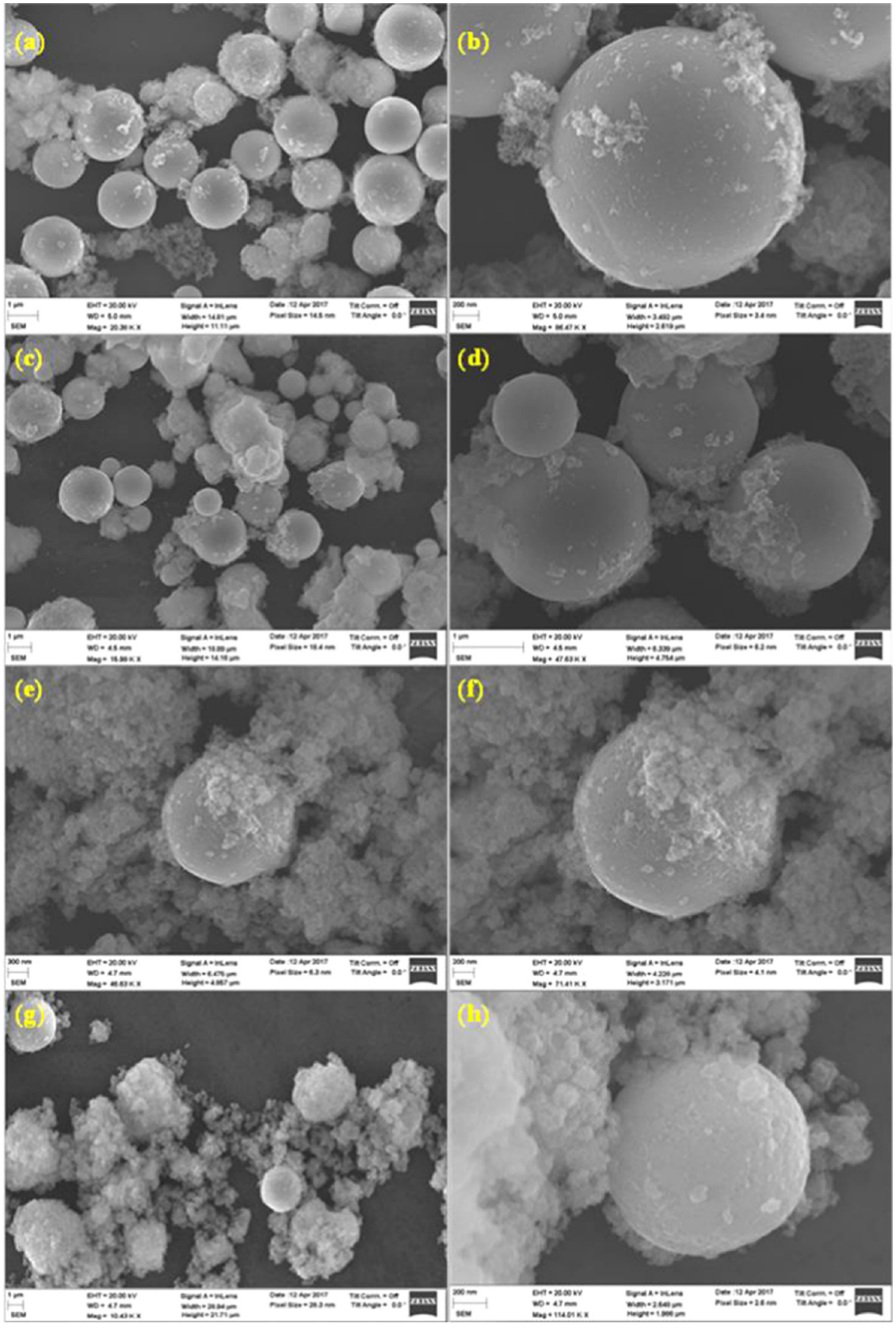


**Figure 4.** FESEM images and enlarged views of (a, b) BBMO; (c, d) CBBMO-1; (e, f) CBBMO-3; and (g, h) CBBMO-5.

*3.9.1. Mott–Schottky Analysis.* To check the photocatalytic activity of the prepared composite toward degradation of phenol and reduction of hexavalent chromium, favorable band alignment is necessary for the flow of charge carriers and formation of the active radicals. To evaluate experimentally the band edge positions, Mott–Schottky analysis is carried out, and



DOI: 10.1021/acsomega.7b01250
*ACS Omega* 2017, 2, 9040–9056

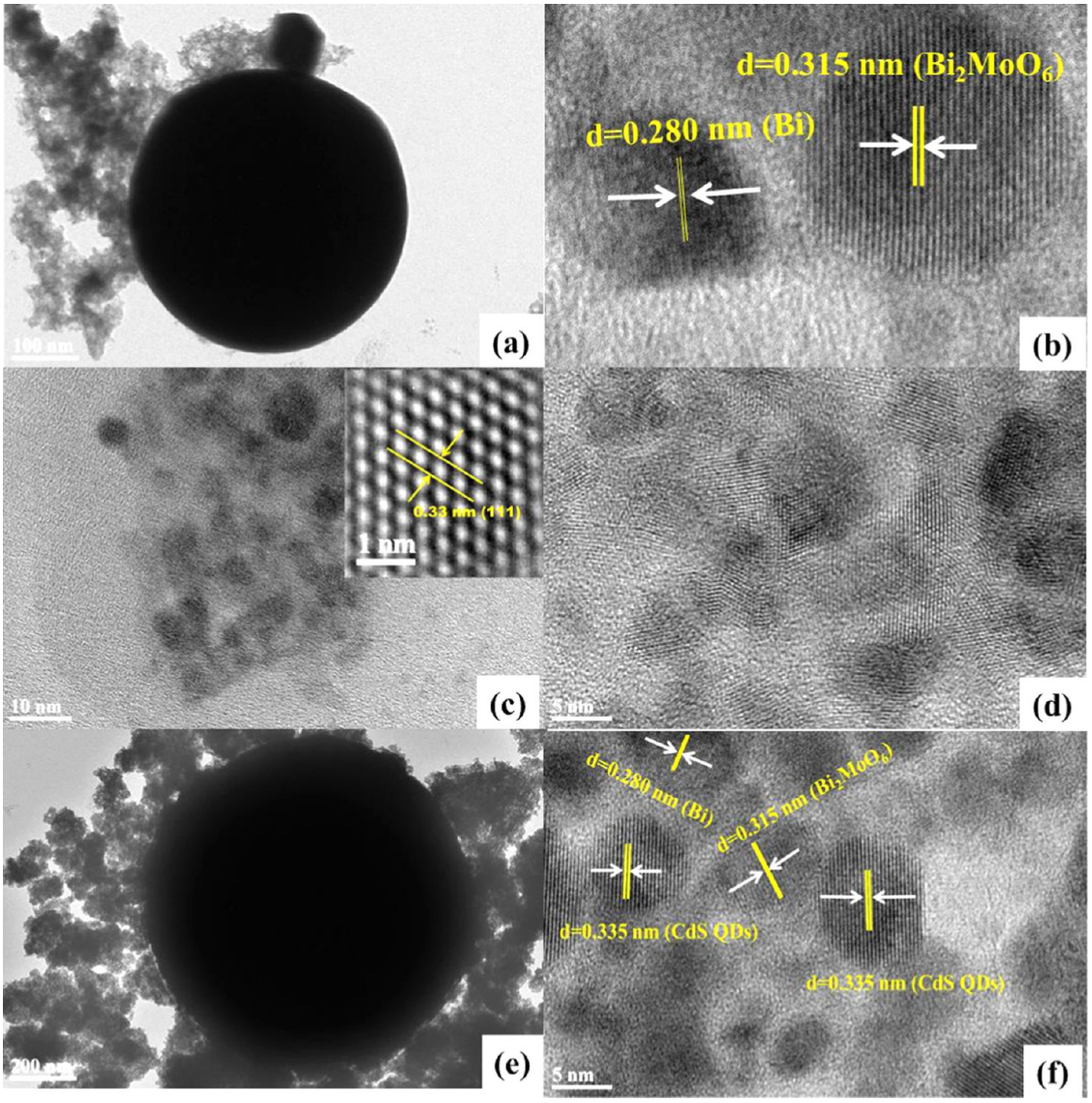


**Figure 5.** TEM and HRTEM images of (a, b) BBMO; (c, d) CdS QDs; and (e, f) CBBMO-3.

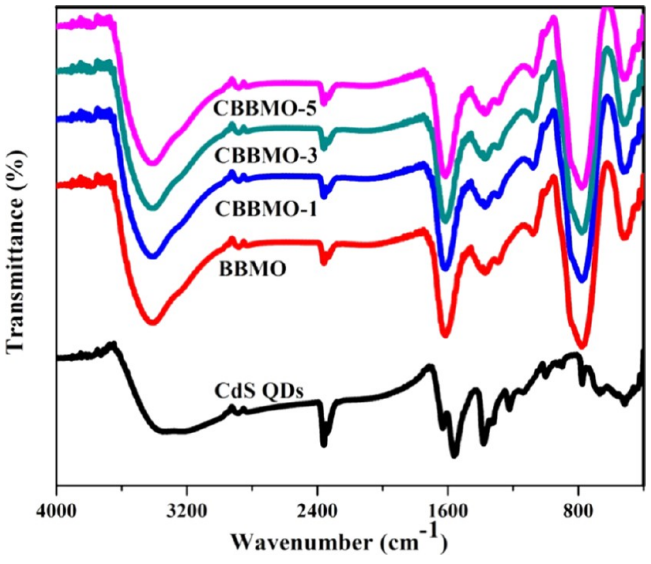


**Figure 6.** FTIR spectra of BBMO and the prepared composites.

the Mott−Schottky plots of bare bismuth molybdate (BMO) and CdS QDs are given in Figure 8a,b.

The graph is plotted by taking inverse of the square of measured space charge capacitance ($C_{SC}$) in unit of Farad (F) as ordinate and the applied potential ($V_{app}$) in volt (V) as abscissa using the following equation (eq 3).

$$C_{SC}^{-2} = \frac{2(V_{app} - V_{fb} - (kT/e))}{N_D \varepsilon \varepsilon_0 e A^2} \quad (3)$$

where $V_{fb}$ is the flat band potential, which is calculated by the extrapolation of the graph and intersection point of abscissa, and $k$, $T$, $e$, $N_D$, $\varepsilon$, $\varepsilon_0$, and $A$ are the Boltzmann constant in J $K^{-1}$, absolute temperature in K, electronic charge in C, donor density in $cm^3$, semiconductor dielectric constant, dielectric constant in vacuum, and area in $cm^2$, respectively. The slope of this equation can also be helpful in calculating the value of $N_D$ if the values of $\varepsilon$ and $A$ are known. The positive slope of the plot reveals the obvious n-type behavior for both BMO and CdS QDs, and the intersection point is independent of applied frequency. It is very well known that the Mott−Schottky plot is representative of the flat band potential of the semiconductor.



DOI: 10.1021/acsomega.7b01250
ACS Omega 2017, 2, 9040−9056

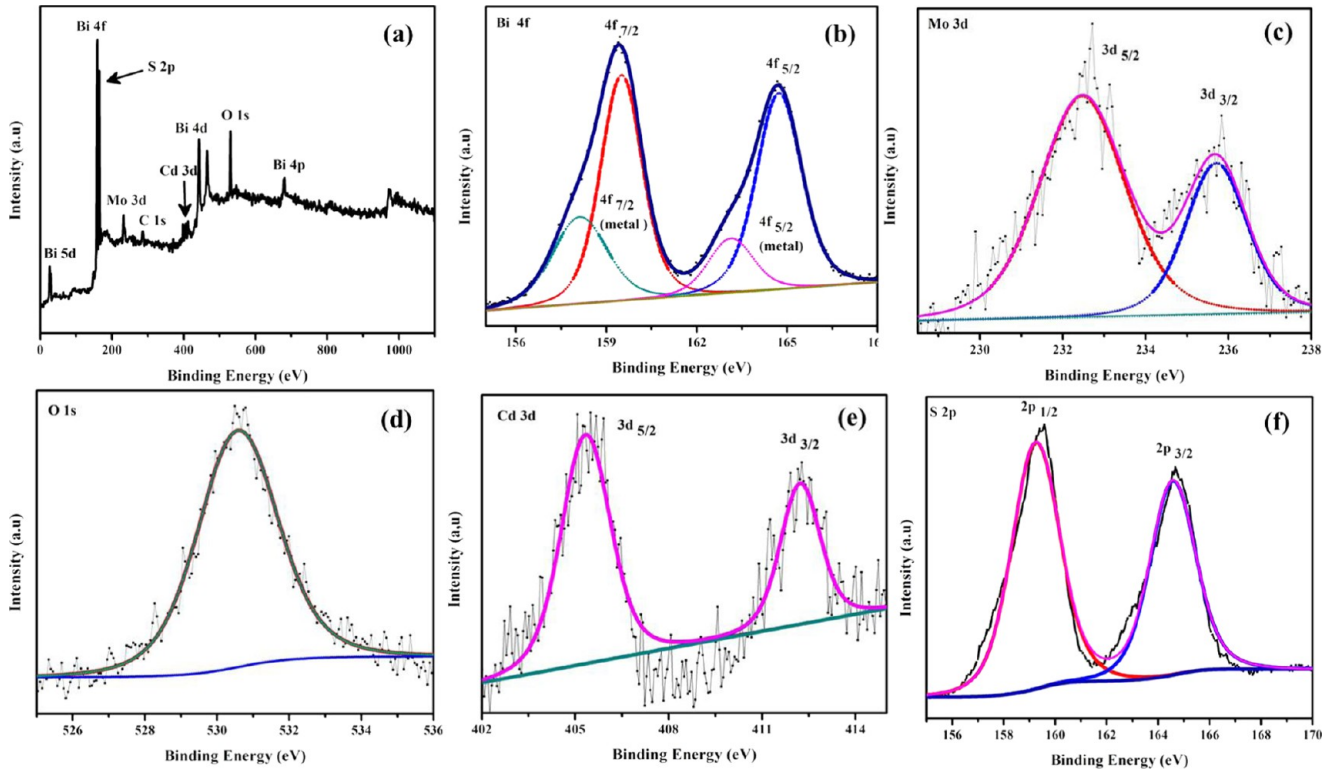


**Figure 7.** XPS images of (a) survey scan of CBBMO-3, (b) Bi 4f, (c) Mo 3d, (d) O 1s, (e) Cd 3d, and (f) S 2p.

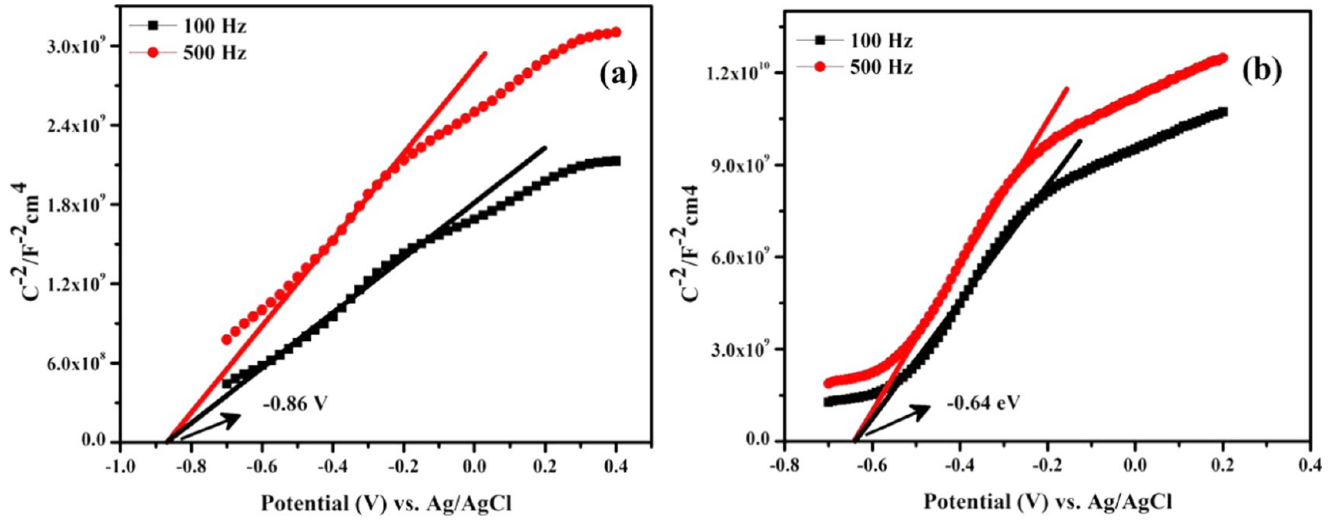


**Figure 8.** Mott–Schottky plots of (a) BMO and (b) CdS QDs.

Negative flat band potential of −0.86 and −0.63 V versus Ag/AgCl is found for both BMO and CdS QDs. The flat band potential in NHE scale is calculated to be −0.31 and −0.08 V for BMO and CdS QDs, respectively. As the conduction band of n-type semiconductors is 0.1 V more negative than the flat band potential,[31] the CB edge potential of BMO and CdS are at −0.40 and −0.18 V (vs NHE). Hence, the valence band potential of BMO and CdS QDs is calculated to be +2.08 and +2.11 V, respectively.

*3.9.2. Linear Sweep Voltammetry.* The typical n-type behavior is represented here from the increasing anodic current density, which has been increased with applied positive potential. As shown in Figure 9a, under dark condition, BBMO shows 0.14 mA/cm$^2$ of photocurrent density, and there is enhancement of the photocurrent value in case of CBBMO composites. With the increase of loading content of CdS QDs from CBBMO-1 to CBBMO-3, there is a steady enhancement of photocurrent density, but after that, 5 wt % loading amount of CdS QDs inhibits the increment of photocurrent generation.

Under dark condition, maximum 0.58 mA/cm$^2$ of current was generated by CBBMO-3 composite. But the CBBMO-3 photoanode under front-side photoillumination could generate 0.8 mA/cm$^2$ of current at the applied potential.

*3.9.3. Electrochemical Impedance Spectroscopy.* Figure 10 shows the Nyquist plot ($Z_{img}$ vs $Z_{real}$), which is a measure of intrinsic electrical properties, especially conductivity. The idea about conductivity or charge-transfer resistance can be easily best evaluated from the radius of the semicircle. The smaller the



DOI: 10.1021/acsomega.7b01250
ACS Omega 2017, 2, 9040−9056

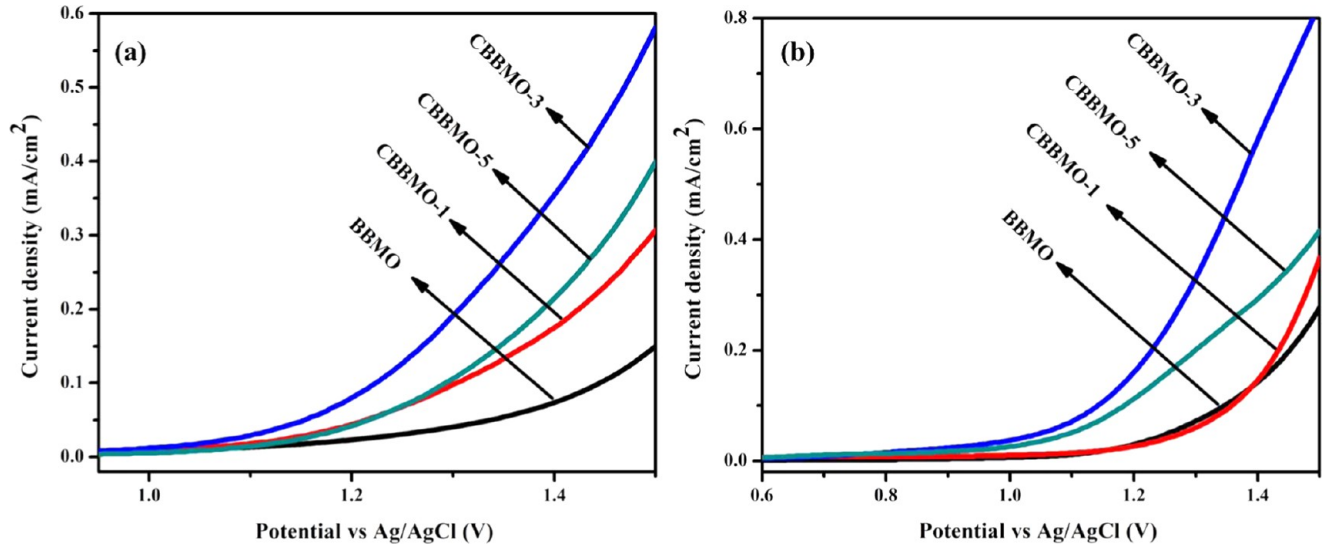


**Figure 9.** *J*–*E* curves under (a) dark and (b) light conditions of BBMO and CBBMO composites coated on FTO measured in 0.1 M $Na_2SO_4$.

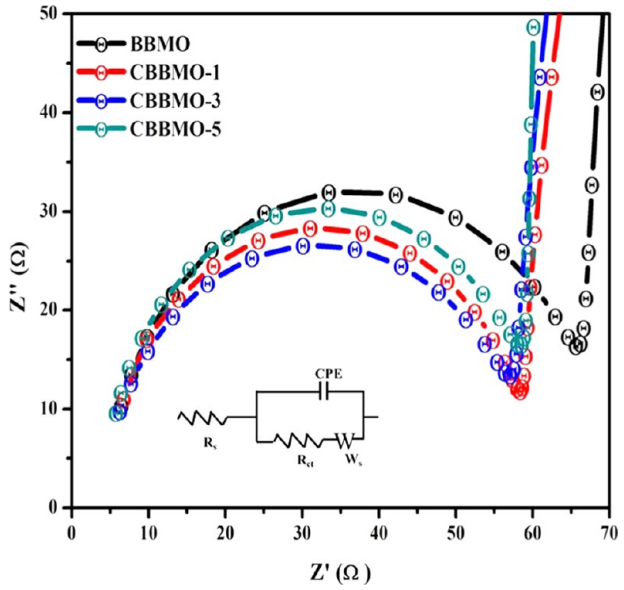


**Figure 10.** Nyquist plot of BBMO and CBBMO composites in the frequency range of 100–95 000 Hz.

radius of semicircle, the better is the conductivity of the semiconductor, which is CBBMO-3 in our case. This is also well supported by the catalytic activity, which will be discussed later. The values of charge-transfer resistance of the prepared samples follow the order: CBBMO-3 (50.00 Ω) < CBBMO-5 (51.22 Ω) < CBBMO-1 (52.34 Ω) < BBMO (58.74 Ω). The plot was fitted with the circuit model, which consists of $R_s$, $R_{ct}$, $W_s$, and CPE, where $R_s$ is the ohmic series resistance (charge-transfer resistance and contact resistance at electrolyte/electrode), $R_{ct}$ is the electron-transfer resistance for the reaction, $W_s$ is the Warburg resistance, and CPE is the constant phase element.

**3.10. Determination of Point of Zero Charge.** The surface charge is a key point in the reduction of Cr(VI) as Cr species in anionic form get attracted by the catalyst surface. For this, the catalyst surface should be positively charged and hence to determine the surface charge of catalyst, drift method[15] is used. This method is useful to calculate the point of zero charge (PZC) of prepared samples. The typical procedure involves the preparation of 0.005 M NaCl aqueous solution, followed by boiling to remove dissolved $CO_2$. The pH of the solution was maintained at 2, 4, 6, and 8 by 0.5 M HCl and 0.5 M NaOH. In the next step, 20 mL of the above-prepared solution with 0.02 g of CBBMO-3 was stirred for 24 h to attain the adsorption–desorption equilibrium. Then, the final pH of a required solution is plotted against the pH of the solution before treatment. This graph (Figure 11) results a pH value of $pH_{initial}$ = $pH_{final}$, which is called the point of zero charge ($pH_{PZC}$). The consensus is that if the pH is less than the $pH_{PZC}$, the surface of catalyst is positively charged, and if the pH succeeds $pH_{PZC}$, the surface becomes negatively charged.[15]

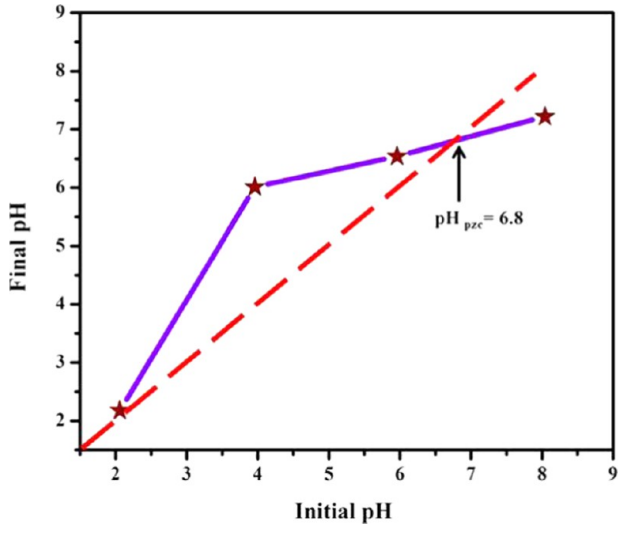


**Figure 11.** Drift method of calculation of $pH_{PZC}$ of CBBMO-3.

## 4. PHOTOCATALYTIC ACTIVITY

**4.1. Photocatalytic Reduction of Cr(VI).** Due to the wide-range light absorption ability and photostability of CBBMO, it was utilized to reduce toxic Cr(VI). Its photocatalytic nature was due to certain control experimental conditions. During the reaction, there is no significant



DOI: 10.1021/acsomega.7b01250
ACS Omega 2017, 2, 9040–9056

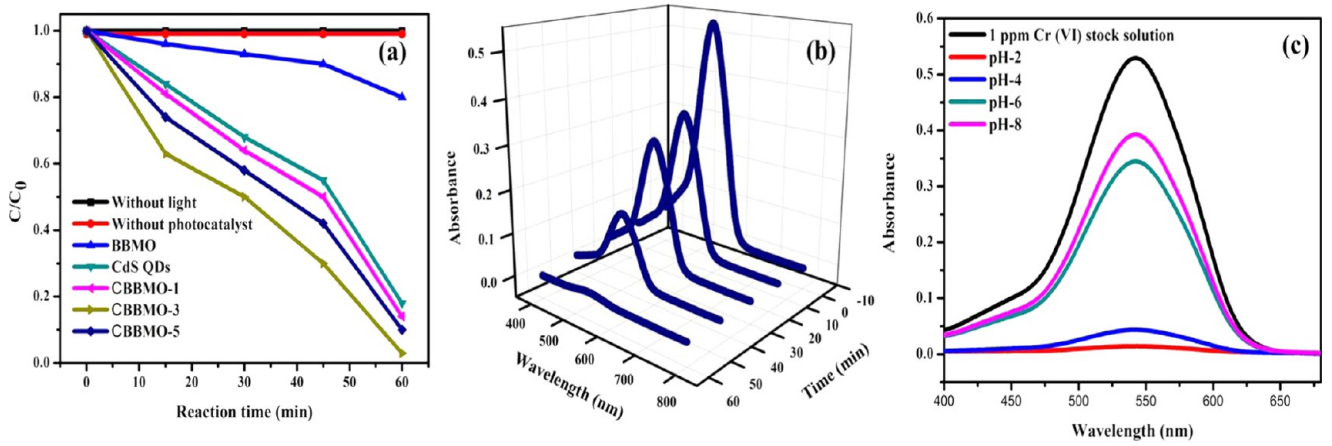


**Figure 12.** (a) Photocatalytic reduction of Cr(VI); (b) spectral changes during reduction of Cr(VI) over CBBMO-3 at various intervals of time; and (c) spectral changes during reduction of Cr(VI) at different pHs.

**Table 3. Comparison Study on Reduction of Cr(VI) and Phenol Degradation over other Photocatalysts**

| catalyst | concentration of Cr(VI) solution/phenol | light source | reaction time (min) | pH | result (%) | ref |
|---|---|---|---|---|---|---|
| $\alpha$-$MnO_2$@RGO | 10 mg/L Cr | visible light | 120 | 2 | 97 | 14 |
| P-doped porous ultrathin g-$C_3N_4$ nanosheets | 20 mg/L Cr | visible light | 120 | 2.13 | 75 | 32 |
| N, S co-doped $CeO_2$ | 50 mg/L Cr | visible light | 120 | 2 | 93 | 33 |
| $Ag_2S$ QDs/$SnS_2$ | 50 mg/L Cr | visible light | 60 | | 57 | 34 |
| Bi/$Bi_2MoO_6$ | 100 mg/L Cr | visible light | 60 | 2 | 97 | this study |
| Au-Pd/rGO | 0.5 mM phenol | sunlight | 300 | 6.9 | 94.45 | 35 |
| $TiO_2$ nanotube array | 20 mg/L phenol | UV light | 400 | | 75 | 36 |
| Pt and $Na_2CO_3$ on $TiO_2$ | 0.43 mM phenol | UV light | 60 | 8 | 60 | 37 |
| Bi/$Bi_2MoO_6$/CdS QDs | 10 ppm phenol | solar light | 60 | 6 | 47 | this study |

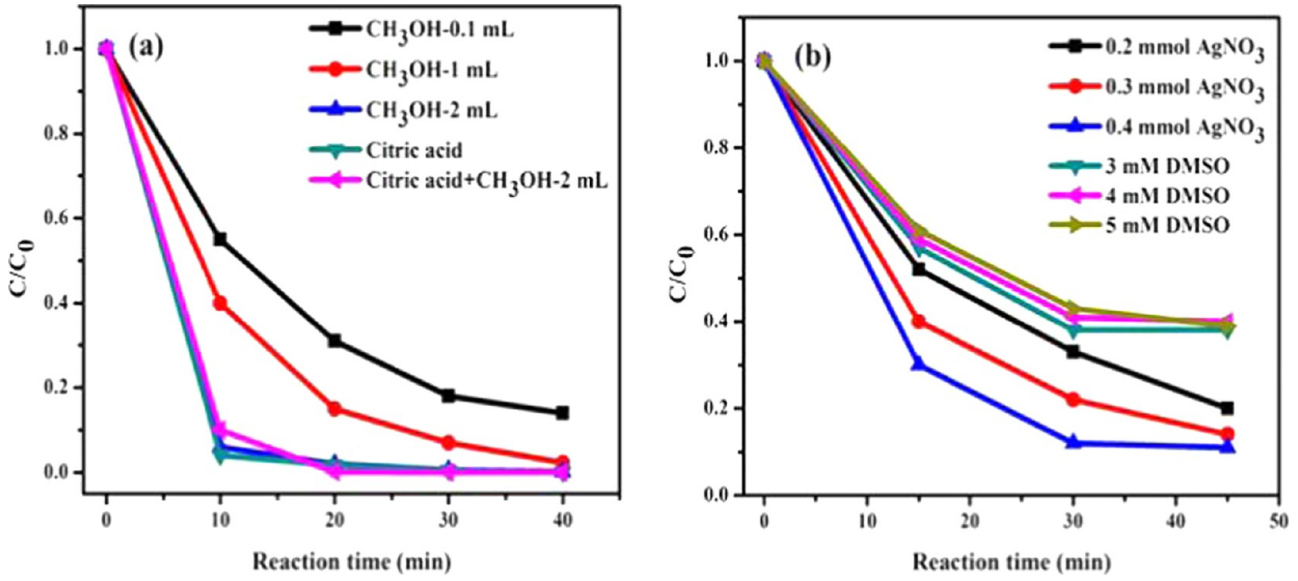


**Figure 13.** Control experimental conditions involving different (a) hole and (b) electron scavengers.

reduction of Cr(VI) in the absence of either light or catalyst (Figure 12a), which confirms the admirable stability of $K_2Cr_2O_7$ solution. As shown in Figure 12a, 20 and 82% reduction was observed by neat BBMO and CdS QDs, respectively. Interestingly, the rate of reduction was greatly enhanced after loading of CdS QDs on BBMO. It was observed that by the end of the reaction period, CBBMO-3 could reduce 97% of hexavalent Cr in 1 h. The Cr remediation efficiencies of the other prepared composites are 86, 97, and 90% over CBBMO-1, CBBMO-3, and CBBMO-5, respectively. This result shows the best photocatalytic activity of CBBMO-3 toward the photocatalytic reduction of hexavalent Cr in comparison to the other reported work (Table 3). The spectral changes during the removal of Cr(VI) over all prepared catalysts were tested at various intervals of time and are represented in Figure 12b.

*4.1.1. Effect of pH on Cr(VI) Reduction.* pH plays a very essential role in the reduction of hexavalent Cr; hence, to



DOI: 10.1021/acsomega.7b01250
ACS Omega 2017, 2, 9040−9056

investigate its influence, a series of experiments were performed at pHs 2, 4, 6, and 8. The pictorial representation is shown in Figure 12c, which indicates that the suitable pH value is 2. On this basis, the entire experiment toward photocatalytic removal of Cr(VI) was carried out at pH 2. The lower pH value is maintained as reaction condition because, at this pH, Cr is predominantly present in anionic form, i.e., as $Cr_2O_7^{2-}$, and it is quite less than the $pH_{PZC}$ value ($pH_{PZC}$ = 6.8). As mentioned earlier, if the pH is less than $pH_{PZC}$, the CBBMO surface is positively charged, resulting in effective interaction between catalyst surface and $Cr_2O_7^{2-}$, which is a suitable condition for the removal of hexavalent Cr. The reduction of Cr(VI) to Cr(III) proceeds as per the following equation.

$$Cr_2O_7^{2-} + 14H^+ + 6e^- \rightarrow 2Cr^{3+} + 7H_2O \quad (4)$$

From this equation, it is clear that due to plethora of protons available the photocatalytic activity is encouraged at lower pH.

*4.1.2. Confirmation of Cr(VI) to Cr(III).* After the experiment, Cr(VI) was reduced to Cr(III), and this was analyzed by $KMnO_4$. To verify the existence of nontoxic Cr(III), $KMnO_4$ solution was used to oxidize Cr(III) back to Cr(VI), which was confirmed colorimetrically by the DPC method.[15] In a typical experiment, 0.02 M $KMnO_4$ aqueous solution was prepared, 0.1 mL of which was added to 1.9 mL of the residual solution after irradiated with sunlight for 1 h, and the same DPC method was used for the detection of concentration for Cr(VI). From the above experiment, it is clear that Cr(VI) is reduced to Cr(III).

**4.2. Detection of Active Species.** As it is known that electrons in CB of catalysts are the active species for Cr(VI) reduction, to prove this, methanol can be used as hole scavenger, which reacts with the photoinduced holes in the VB of the catalysts to achieve fast photocatalytic reduction of Cr(VI). The typical procedure involves addition of various amounts of $CH_3OH$ and citric acid to the acidic Cr(VI) solution at pH 2.

Figure 13a depicts that the addition of methanol decreases the photoreduction time and makes it a fast photocatalytic removal of hexavalent Cr. In addition to methanol, 1 mL of aqueous citric acid solution (1 g/10 mL) was also used to completely reduce Cr(VI) within 40 min. Complete reduction of Cr(VI) was observed in 20 min when both methanol (2 mL) and citric acid (1 mL) were in the reaction medium. This suggests that the main active species may be electron; this statement has also been proved by taking various amounts of $AgNO_3$ and dimethyl sulfoxide (DMSO) as electron scavenger, as shown in Figure 13b. As shown in the figure, 0.2 mmol $AgNO_3$ shows higher electron-trapping capacity than 0.3 and 0.4 mmol $AgNO_3$. But, it was observed that the electron-trapping ability of DMSO is higher compared to $AgNO_3$. It was studied experimentally that 4 mM DMSO is sufficient compared to 3 and 5 mM DMSO to scavenge the photoexcited electrons. Still some reduction occurred, which will be discussed in Section 4.4.

*4.2.1. Kinetics Followed by CBBMO-3 in Cr(VI) Reduction.* Zero-order kinetics (Figure 14) was followed by CBBMO for the reduction of Cr(VI), which was concluded by fitting the experimental data with zero-, first-, and second-order kinetics model equations (eqs 5−7). The obtained fitting results, i.e., slope (rate constant, $k$), coefficient of determination, $R^2$, and standard error, are tabulated in Table 4.

$$C = -k_0 t + C_0 \quad (5)$$

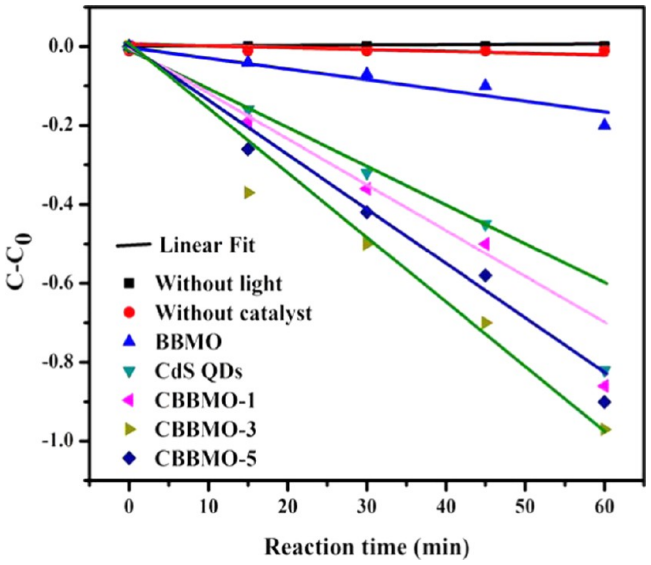


**Figure 14.** Zero-order kinetics followed by reduction of Cr(VI) over CBBMO-3.

$$\frac{C}{C_0} = e^{-k_1 t} \quad (6)$$

$$\frac{1}{C} = \frac{1}{C_0} + k_2 t \quad (7)$$

Here, $C_0$ and $C$ are concentrations of Cr(VI) at time = 0 and $t$, respectively, in mg/L, and $k_0$, $k_1$, and $k_2$ are zero-, first-, and second-order rate constants in mg/L min, $min^{-1}$, and L/mg min, respectively.

**4.3. Photocatalytic Degradation of Phenol.** The versatile photocatalytic activity of CBBMO samples was investigated by degrading 10 ppm phenol as model organic environmental pollutant. Figure 15a shows spectral presentation of phenol degradation under solar light irradiation, and it was measured by a UV−vis spectrometer at ca. 269 nm. The effect of pH was also checked in this process, and pH 6 was found to be a suitable condition for the degradation. The degradation activity follows the sequence as pH 6 > pH 2 > pH 4 > pH 8 (Figure 15b). So, pH 6 was taken as the optimum pH condition to carry out further experiment, and 47.5% phenol was degraded in the presence of CBBMO-3 under solar light in 60 min.

The kinetics through which the phenol degradation mechanism was performed is shown in Figure 15c. The kinetics process involves 0.02 g of CBBMO-3 at pH 6, and the same procedure was surveyed to investigate the kinetics. Results showed that it is the second-order kinetics followed by the degradation process. The symbols in this equation bear their usual meaning. Figure 15d indicates the second-order rate constants; when examined, it was observed that CBBMO-3 possesses a higher rate constant of 0.014 L/mg min, which is 14 and 7 times higher than that of the CBBMO-1 (0.001 L/mg min) and CBBMO-5 (0.002 L/mg min) composites, respectively. The conclusion drawn from the observation is that CBBMO-3 catalyst accelerates the photodegradation of 10 ppm phenol compared to all other prepared samples.

**4.4. Mechanism Involved in Cr(VI) Reduction and Phenol Degradation.** All of the above experimental procedure directs the following acceptable mechanistic pathway



DOI: 10.1021/acsomega.7b01250
ACS Omega 2017, 2, 9040−9056

**Table 4. Fitted Results of Cr(VI) Reduction over CBBMO-3 at pH 2**

| catalysts | CdS QDs | BBMO | CBBMO-1 | CBBMO-3 | CBBMO-5 |
|---|---|---|---|---|---|
| zero order $R^2$ | 0.89 | 0.93 | 0.95 | 0.96 | 0.97 |
| slope ($k_0$) | 0.003 | 0.012 | 0.013 | 0.015 | 0.014 |
| standard error | 0.001 | 0.001 | 0.001 | 0.001 | 0.001 |
| first order $R^2$ | 0.87 | 0.75 | 0.753 | 0.72 | 0.77 |
| slope ($k_1$) | 0.003 | 0.025 | 0.029 | 0.05 | 0.03 |
| standard error | 0.006 | 0.007 | 0.008 | 0.015 | 0.008 |
| second order $R^2$ | 0.84 | 0.54 | 0.52 | 0.41 | 0.5 |
| slope ($k_2$) | 0.0038 | 0.064 | 0.087 | 0.442 | 0.126 |
| standard error | 0.028 | 0.026 | 0.03 | 0.022 | 0.056 |

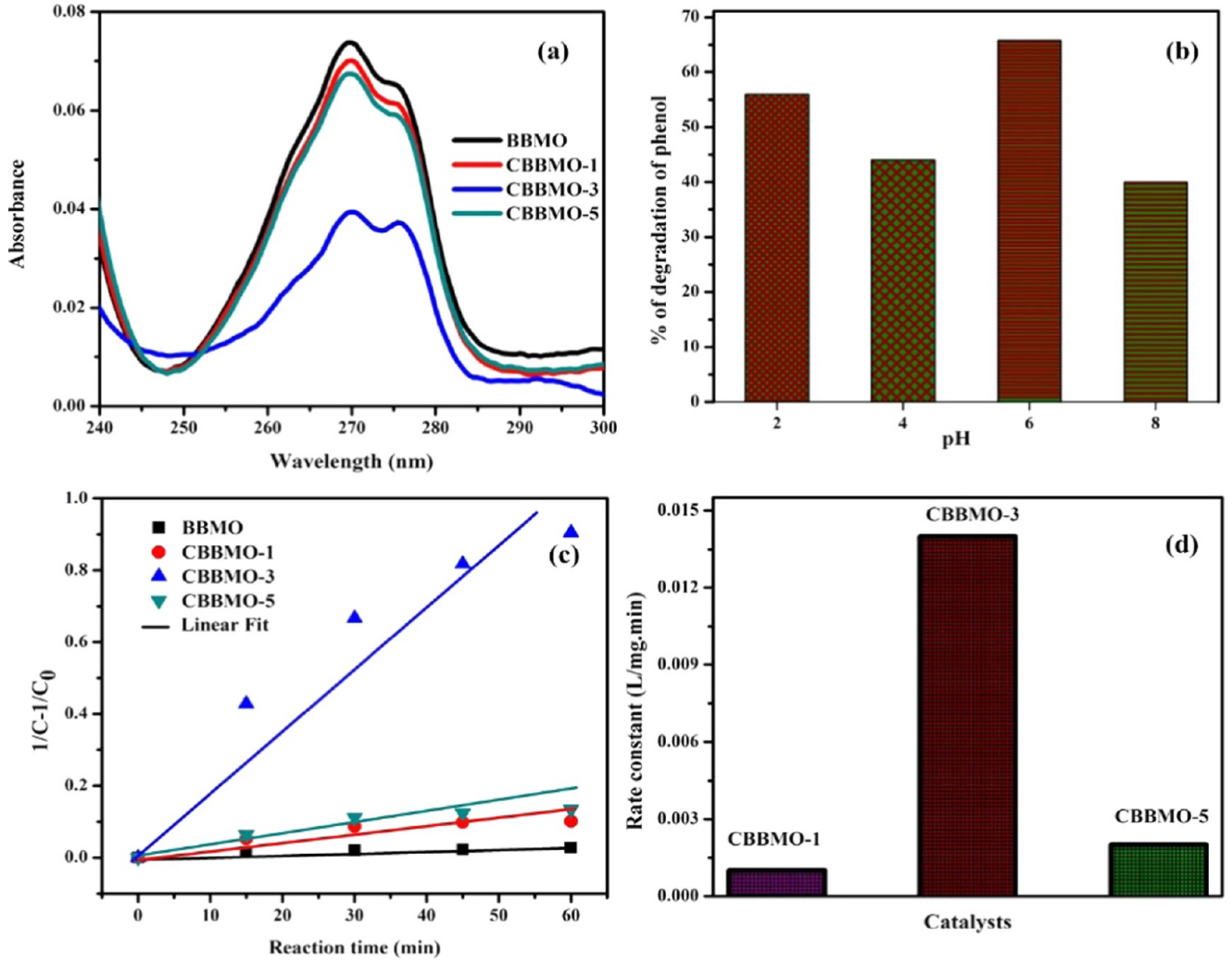


**Figure 15.** (a) Absorption spectra of prepared catalysts in phenol degradation; (b) comparison of rate of degradation of phenol by CBBMO-3 at different pHs; (c) second-order kinetics observed in the degradation process; and (d) histogram representing the comparison of second-order rate constants of prepared samples at pH 6.

for the reduction of Cr(VI) and degradation of phenol, which is embodied in Scheme 1. CdS QDs and Bi in CBBMO-3 act here as the absorption center due to their high absorption capacity and SPR property, respectively. In addition to this, the obtained Brunauer–Emmett–Teller (BET) surface area data of the as-prepared samples (Table S1 of SI) and their respective photocatalytic activities signify that surface area is not the whole criteria in deciding the efficiency of photocatalysts.[38] Rather than charge separation efficiency, light absorption capacity, band gap, band edge potential, active sites, and photostability are key factors in determining the photocatalytic efficiency of the material.

Upon solar light irradiation, photoinduced electrons and holes get separated. As a result of this, holes are in VB, whereas electrons are in CB of BBMO and CdS QDs. As per the CB edge positions of involved semiconductors, electrons migrate from CB of both BMO and CdS QDs to Fermi level of Bi (−0.17 V),[11] meanwhile holes transfer from VB of BMO to CdS QDs and eventually oxidize the hole scavenger (methanol, citric acid) to $CO_2$, $H_2O$, and other mineralized products. At



DOI: 10.1021/acsomega.7b01250
ACS Omega 2017, 2, 9040−9056

**Scheme 1. Schematic Presentation of Reduction of Cr(VI) and Degradation of Phenol over CBBMO-3**

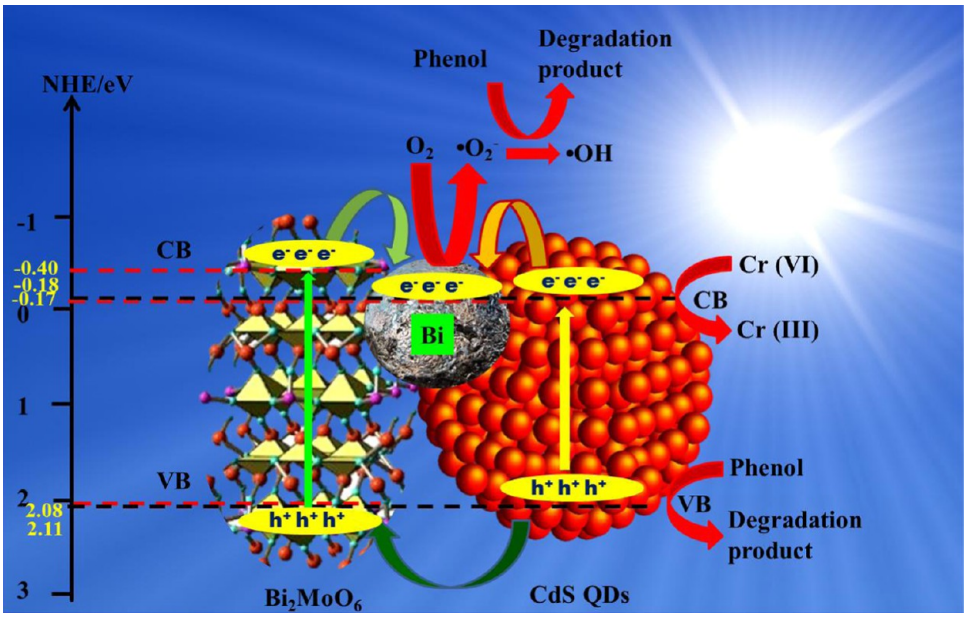


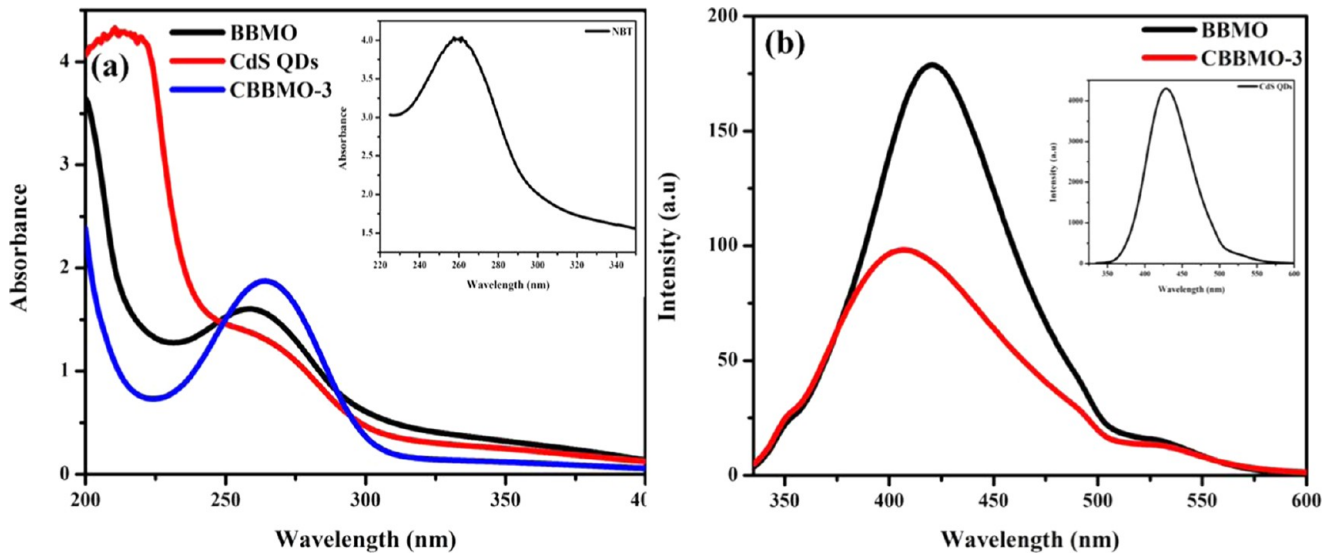


**Figure 16.** Absoption spectra of (a) NBT in neat and CBBMO-3 sample and (b) fluorescence spectra of BBMO and CBBMO-3 in basic solution of $5 \times 10^{-5}$ M terephthalic acid.

the surface of Bi, some migrated electrons are utilized to reduce Cr(VI) as per eq 4 and some electrons are engaged in the production of superoxide radicals ($^{\bullet}O_2^-$), which indirectly reduce Cr(VI) to Cr(III) through a two-step process.[39] As $E_0$ ($O_2/^{\bullet}O_2$) = −0.046 eV versus NHE,[39] which is less negative than the CB potential value of BMO, CdS QDs, and Bi, electrons are transferred to generate $^{\bullet}O_2^-$. This mechanism is proposed because even in the presence of DMSO ($e^-$ scavenger), CBBMO-3 could reduce 60% Cr(VI); hence, it is supposed that $^{\bullet}O_2^-$ is also participating in Cr(VI) reduction. The generation of $^{\bullet}O_2^-$ is confirmed from the NBT (nitroblue tetrazolium chloride) test.[40] In CBBMO-3, less $^{\bullet}O_2^-$ are formed compared to the neat materials, which is confirmed from the high absorbance value from Figure 16a. So, partial involvement of $^{\bullet}O_2^-$ is confirmed from this NBT test.

From the scavenger test of phenol, it was concluded that the major active species behind this is $^{\bullet}OH$ and the minor species is $^{\bullet}O_2^-$. In neutral and basic medium, $^{\bullet}O_2^-$ formation is favorable, whereas the formation of $H_2O^{\bullet}$ is favorable in acidic medium. Both the species are responsible for the generation of $^{\bullet}OH$ radical.[35] The confirmation of production of these radicals is graphically presented in Figure 16a,b. The formation and role of $^{\bullet}O_2^-$ is similar in this regard, as explained previously. The formation of $^{\bullet}OH$ radical might be proposed in two ways. One is direct formation from holes at VB of CdS QDs because $E_0$ ($OH^-/^{\bullet}OH$) = 1.99 versus NHE[32] and the other is indirect formation via $H_2O_2$, as proposed in the following equations.

$$\text{CBBMO-3} + h\nu \rightarrow \text{Bi}(e^-) + \text{BMO}(h^+) + \text{CdS}(h^+)$$

$$\text{Bi}(e^-) + O_2 \rightarrow {}^{\bullet}O_2^-$$

$$\text{Bi}(e^-) + {}^{\bullet}O_2^- + H_2O \rightarrow H_2O^{\bullet} + OH$$

$$\text{Bi}(e^-) + H_2O^{\bullet} \rightarrow H_2O_2$$



DOI: 10.1021/acsomega.7b01250
ACS Omega 2017, 2, 9040−9056

$$H_2O_2 + Bi(e^-) \rightarrow {}^{\bullet}OH + OH^-$$

$$BMO(h^+) + CdS(h^+) + H_2O \rightarrow {}^{\bullet}OH + H^+$$

$$\text{phenol} + {}^{\bullet}O_2^- \rightarrow \text{degradation}$$

$$\text{phenol} + {}^{\bullet}OH \rightarrow \text{degradation}$$

The resultant degradation reaction is phenol + ${}^{\bullet}O_2^-$ + ${}^{\bullet}OH$ → degradation

**4.5. Stability and Reusability of CBBMO Composite.** For the practical application (wastewater remediation) of this catalyst, the stability must be retained so that it can be reused several times. Figure 17 shows the repeated use of this catalyst up to five cycles of Cr(VI) reduction and phenol degradation. Average reduction and degradation of Cr(VI) and phenol of 95.76 and 47% are maintained, respectively, for five cycles. CBBMO-3 obtained after Cr(VI) reduction was characterized by FTIR analysis, and it is very prominent from Figure 18a that there is shifting of peak toward lower wavenumber. This is an indication of good interaction between CBBMO-3 and Cr(VI). Even after five cycles of treatment in Cr(VI), the characteristic peaks still persist. Additionally, UV-DRS spectra (Figure 18b) are also provided here, which conclude little change in absorption region after reduction of Cr(VI).

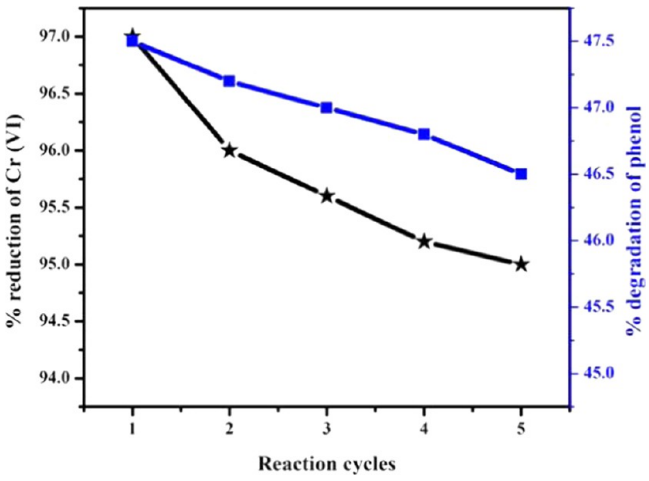


**Figure 17.** Cr(VI) reduction and phenol degradation efficiency versus reaction cycles of CBBMO-3.

## 5. CONCLUSIONS

A systematic methodology has been followed to evaluate the versatile photocatalytic efficiency of the prepared composite (CBBMO-3) for Cr(VI) reduction and phenol degradation. Comparative study of using different hole scavengers has also been investigated, which significantly reduces the reaction time to achieve the target. The zero- and second-order kinetics are followed by reduction of Cr species and degradation of phenol, respectively. Cr(VI) removal and phenol degradation efficiencies are found to be 97 and 47.5%, respectively, over CBBMO-3. From the scavenger test, electron is found to be the main key active species, ${}^{\bullet}O_2^-$ is partially involved in the reduction of Cr(VI), and the lion's share goes to both ${}^{\bullet}O_2^-$ and ${}^{\bullet}OH$ in the degradation of phenol. The present work suggests that low-cost Bi acts as a substitute for noble metals and CdS QDs greatly enhance the photocatalytic activity. This work possibly provides industrial applications toward removal of Cr(VI) and degradation of phenol.

## ■ ASSOCIATED CONTENT

### Supporting Information

The Supporting Information is available free of charge on the ACS Publications website at DOI: 10.1021/acsomega.7b01250.

PL and PLE spectra of CBBMO-3, FTIR spectra of pure TGA and TGA-capped CdS QDs (Figures S1 and S2), and BET surface area data of the prepared composites (Table S1) (PDF)

## ■ AUTHOR INFORMATION

### Corresponding Authors

*E-mail: satyabadimartha@soauniversity.ac.in (S.M.).

*E-mail: kulamaniparida@soauniversity.ac.in, paridakulamani@yahoo.com. Tel: +91-674-2351777. Fax: +91-674-2350642 (K.M.P.).

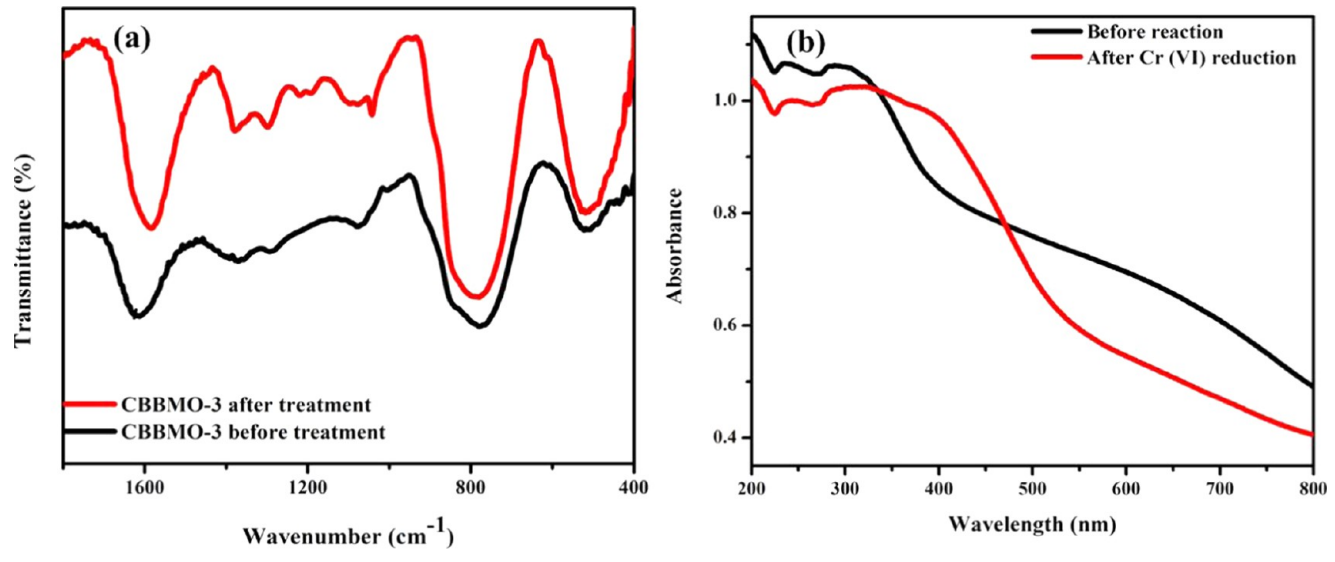


**Figure 18.** (a) FTIR spectra and (b) UV-DRS spectra of CBBMO-3 before and after reduction of Cr(VI) at pH 2.



DOI: 10.1021/acsomega.7b01250
ACS Omega 2017, 2, 9040−9056

**ORCID**

Arun Thirumurugan: 0000-0001-7261-988X
K. M. Parida: 0000-0001-7807-5561

### Notes

The authors declare no competing financial interest.

## ■ ACKNOWLEDGMENTS

The authors gratefully acknowledge the SOA University management for their support and encouragement. They are obliged to Prof. P.V. Satyam, IOP, Bhubaneswar, for his support in SEM and TEM analyses. They also acknowledge the American Chemical Society for funding through ACS authors reward.

## ■ REFERENCES

(1) Han, B.; Zhang, J.; Li, P.; Li, J.; Bian, Y.; Shi, H. Synthesis and Luminescence Properties of $Eu^{3+}$ Doped High Temperature Form of $Bi_2MoO_6$. *J. Electron. Mater.* **2015**, *44*, 1028−1033.

(2) Zhou, D.; Wang, H.; Yao, X.; Pang, L. Microwave Dielectric Properties of Low Temperature Firing $Bi_2Mo_2O_9$ Ceramic. *J. Am. Ceram. Soc.* **2008**, *91*, 3419−3422.

(3) Zhou, D.; Randall, C. A.; Wang, H.; Pang, L.; Yao, X. Microwave Dielectric Ceramics in $Li_2O$−$Bi_2O_3$−$MoO_3$ System with Ultra-Low Sintering Temperatures. *J. Am. Ceram. Soc.* **2010**, *93*, 1096−1100.

(4) Lou, S. N.; Scott, J.; Iwase, A.; Amal, R.; Ng, Y. H. Photoelectrochemical Water Oxidation using a $Bi_2MoO_6$/$MoO_3$ Heterojunction Photoanode Synthesised by Hydrothermal Treatment of an Anodised $MoO_3$ Thin Film. *J. Mater. Chem. A* **2016**, *4*, 6964−6971.

(5) Theobald, F.; Laarif, A.; Hewat, A. W. Redetermination of the Crystal Structure of $\alpha$-$Bi_2O_3$•3 $MoO_3$ by Neutron Diffraction and the Catalytic Oxidation of Propene. *Mater. Res. Bull.* **1985**, *20*, 653−665.

(6) Chen, H. Y.; Sleight, A. W. Crystal Structure of $Bi_2Mo_2O_9$: A Selective Oxidation Catalyst. *J. Solid State Chem.* **1986**, *63*, 70−75.

(7) Teller, R. G.; Brazdil, J. F.; Grasselli, R. K. The Structure of $\gamma$-Bismuth Molybdate, $Bi_2MoO_6$, by Powder Neutron Diffraction. *Acta Crystallogr.* **1984**, *C40*, 2001−2005.

(8) Vieira Soares, A. P.; Dimitrov, L. D.; de Oliveira, M. C. R. A.; Hilaire, L.; Portela, M. F.; Grasselli, R. K. Synergy Effects between $\beta$ and $\gamma$ Phases of Bismuth Molybdates in the Selective Catalytic Oxidation of 1-butene. *Appl. Catal., A* **2003**, *253*, 191−200.

(9) Yuan, B.; Wang, C.; Qi, Y.; Song, X.; Mu, K.; Guo, P.; Meng, L.; Xi, H. Decorating Hierarchical $Bi_2MoO_6$ Microspheres with Uniformly Dispersed Ultrafine Ag Nanoparticles by an In Situ Reduction Process for Enhanced Visible Light-Induced Photocatalysis. *Colloids Surf., A* **2013**, *425*, 99−107.

(10) Zhang, B.; Li, J.; Gao, Y.; Chong, R.; Wang, Z.; Guo, L.; Zhang, X.; Li, C. To Boost Photocatalytic Activity in Selective Oxidation of Alcohols on Ultrathin $Bi_2MoO_6$ Nanoplates with Pt Nanoparticles as Cocatalyst. *J. Catal.* **2017**, *345*, 96−103.

(11) Zhao, Z.; Zhang, W.; Sun, Y.; Yu, J.; Zhang, Y.; Wang, H.; Dong, F.; Wu, Z. Bi Cocatalyst/$Bi_2MoO_6$ Microspheres Nanohybrid with SPR-Promoted Visible-Light Photocatalysis. *J. Phys. Chem. C* **2016**, *120*, 11889−11898.

(12) Kandi, D.; Martha, S.; Thirumurugan, A.; Parida, K. M. Modification of BiOI Microplates with CdS QDs for Enhancing Stability, Optical Property, Electronic Behavior toward Rhodamine B Decolorization, and Photocatalytic Hydrogen Evolution. *J. Phys. Chem. C* **2017**, *121*, 4834−4849.

(13) Hao, Y.; Dong, X.; Wang, X.; Zhai, S.; Ma, H.; Zhang, X. Controllable Electrostatic Self-Assembly of Sub-3-nm Graphene Quantum Dots Incorporated into Mesoporous $Bi_2MoO_6$ Frameworks: Efficient Physical and Chemical Simultaneous Cocatalysis for Photocatalytic Oxidation. *J. Mater. Chem. A* **2016**, *4*, 8298−8307.

(14) Padhi, D. K.; Baral, A.; Parida, K.; Singh, S. K.; Ghosh, M. K. Visible Light Active Single-Crystal Nanorod/Needle-like $\alpha$-$MnO_2$@RGO Nanocomposites for Efficient Photoreduction of Cr(VI). *J. Phys. Chem. C* **2017**, *121*, 6039−6049.

(15) Kostas, V.; Baikousi, M.; Dimos, K.; Vasilopoulos, K. C.; Koutselas, I.; Karakassides, M. A. Efficient and Rapid Photocatalytic Reduction of Hexavalent Chromium Achieved by a Phloroglucinol Derived Microporous Polymeric Organic Framework Solid. *J. Phys. Chem. C* **2017**, *121*, 7303−7311.

(16) Mansingh, S.; Padhi, D. K.; Parida, K. M. Enhanced Photocatalytic Activity of Nanostructured Fe Doped $CeO_2$ for Hydrogen Production under Visible Light Irradiation. *Int. J. Hydrogen Energy* **2016**, *41*, 14133−14146.

(17) He, T.; Wu, D.; Tan, Y. Fabrication of BiOI/$BiVO_4$ Heterojunction with Efficient Visible-Light-Induced photocatalyticactivity. *Mater. Lett.* **2016**, *165*, 227−230.

(18) Shen, Q.; Ogomi, Y.; Chang, J.; Toyoda, T.; Fujiwara, K.; Yoshino, K.; Sato, K.; Yamazaki, K.; Akimoto, M.; Kuga, Y.; Katayama, K.; Hayase, S. Optical Absorption, Charge Separation and Recombination Dynamics in Sn/Pb Cocktail Perovskite Solar Cells and Their Relationships to Photovoltaic Performances. *J. Mater. Chem. A* **2015**, *3*, 9308−9316.

(19) Jones, D. A.; Lee, J. U. Observation of the Urbach Tail in the Effective Density of States in Carbon Nanotubes. *Nano Lett.* **2011**, *11*, 4176−4179.

(20) Hossain, M. S.; Kabir, H.; Rahmana, M. M.; Hasan, K.; Bashar, M. S.; Rahman, M.; Gafur, M. A.; Islamg, S.; Amri, A.; Jiang, Z. T.; Altarawneh, M.; Dlugogorsk, B. Z. Understanding the Shrinkage of Optical Absorption Edges of Nanostructured Cd-Zn Sulphide Films for Photothermal Applications. *Appl. Surf. Sci.* **2017**, *392*, 854−862.

(21) Sadhanala, A.; Deschler, F.; Thomas, T. H.; Dutton, S. E.; Goedel, K. C.; Hanusch, F. C.; Lai, M. L.; Steiner, U.; Bein, T.; Docampo, P.; Cahen, D.; Friend, R. H. Preparation of Single-Phase Films of $CH_3NH_3Pb(I1-xBrx)_3$ with Sharp Optical Band Edges. *J. Phys. Chem. Lett.* **2014**, *5*, 2501−2505.

(22) Qi, Y.; Kang, R.; Huang, J.; Zhang, W.; He, G.; Yin, S.; Fang, Y. Reunderstanding the Fluorescent Behavior of Four-Coordinate Monoboron Complexes Containing Monoanionic Bidentate Ligands. *J. Phys. Chem. B* **2017**, *121*, 6189−6199.

(23) Di, J.; Xia, J.; Ji, M.; Li, H.; Xu, H.; Li, H.; Chen, R. The Synergistic Role of Carbon Quantum Dots for the Improved Photocatalytic Performances of $Bi_2MoO_6$. *Nanoscale* **2015**, *7*, 11433−11443.

(24) Meng, X.; Zhang, Z. $Bi_2MoO_6$ Co-Modified by Reduced Graphene Oxide and Palladium ($Pd^{2+}$ And $Pd^0$) with Enhanced Photocatalytic Decomposition of Phenol. *Appl. Catal., B* **2017**, *209*, 383−393.

(25) Ashwini, K.; Pandurangappa, C.; Nagabhushana, B. M. Synthesis and Optical Properties of Undoped and Eu-Doped Zns Nanoparticles. *Phys. Scr.* **2012**, *85*, 065706−065710.

(26) Parida, K. M.; Mohapatra, L. Carbonate Intercalated Zn/Fe Layered Double Hydroxide: A Novel Photocatalyst for the Enhanced Photo Degradation of Azo Dyes. *Chem. Eng. J.* **2012**, *179*, 131−139.

(27) Thangadurai, P.; Balaji, S.; Manoharan, P. T. Surface Modification of CdS Quantum Dots using Thiols—Structural and Photophysical Studies. *Nanotechnology* **2008**, *19*, 435708−435715.

(28) Vikraman, A. E.; Josea, A. R.; Jacoba, M.; Kumar, K. G. Thioglycolic acid Capped CdS Quantum Dots as a Fluorescent Probe for the Nanomolar Determination of Dopamine. *Anal. Methods* **2015**, *7*, 6791−6798.

(29) Yang, H.; Jin, Z.; Hu, H.; Lu, G.; Bi, Y. Fabrication and behaviors of CdS on $Bi_2MoO_6$ Thin film photoanodes. *RSC Adv.* **2017**, *7*, 10774−10781.

(30) Feng, Y.; Yan, X.; Liu, C.; Hong, Y.; Zhu, L.; Zhou, M.; Shi, W. Hydrothermal synthesis of CdS/$Bi_2MoO_6$ heterojunction photocatalysts with excellent visible-light-driven photocatalytic performance. *Appl. Surf. Sci.* **2015**, *353*, 87−94.

(31) Saha, S.; Das, G.; Thote, J.; Banerjee, R. Photocatalytic Metal−Organic Framework from CdS Quantum Dot Incubated Luminescent Metallohydrogel. *J. Am. Chem. Soc.* **2014**, *136*, 14845−14851.



DOI: 10.1021/acsomega.7b01250
*ACS Omega* 2017, 2, 9040−9056

(32) Deng, Y.; Tanga, L.; Zeng, G.; Zhua, Z.; Yan, M.; Zhou, Y.; Wang, J.; Liu, Y.; Wang, J. Insight into Highly Efficient Simultaneous Photocatalytic Removal of Cr(VI) and 2,4-Diclorophenol under Visible Light Irradiation by Phosphorus Doped Porous Ultrathin g-$C_3N_4$ Nanosheets from Aqueous Media: Performance and Reaction Mechanism. *Appl. Catal., B* **2017**, *203*, 343−354.
(33) Tian, N.; Huang, H.; Liu, C.; Dong, F.; Zhang, T.; Du, X.; Yu, S.; Zhang, Y. In-Situ Co-Pyrolysis Fabrication of $CeO_2$/g-$C_3N_4$ n-n Type Heterojunction for Synchronously Promoting the Photo-Induced Oxidation and Reduction Properties. *J. Mater. Chem. A* **2015**, *3*, 17120−17129.
(34) Xu, X.; Duan, X.; Yi, Z.; Zhou, Z.; Fan, X.; Wang, Y. Photocatalytic Production of Superoxide Ion in the Aqueous Suspensions of Two Kinds of Zno under Simulated Solar Light. *Catal. Commun.* **2010**, *12*, 169−172.
(35) Darabdhara, G.; Boruah, P. K.; Borthakur, P.; Hussain, N. Reduced Graphene Oxide Nanosheets Decorated with Au-Pd Bimetallic Alloy Nanoparticles towards Efficient Photocatalytic Degradation of Phenolic Compounds in Water. *Nanoscale* **2016**, *8*, 8276−8287.
(36) Mansingh, S.; Padhi, D. K.; Parida, K. M. Enhanced Visible Light Harnessing and Oxygen Vacancy Promoted N, S co-doped $CeO_2$ nanoparticle: A Challenging Photocatalyst for Cr(VI) Reduction. *Catal. Sci. Technol.* **2017**, *7*, 2772−2781.
(37) Liu, J.; Jing, L.; Gao, G.; Xu, Y.; Xie, M.; Huang, L.; Ji, H. Y.; Xie, J.; Li, H. $Ag_2S$ quantum dots in situ coupled to hexagonal $SnS_2$ with enhanced photocatalytic activity for MO and Cr(VI) removal. *RSC Adv.* **2017**, *7*, 46823−46831.
(38) Parida, K. M.; Nashim, A.; Mahanta, S. K. Visible-light driven $Gd_2Ti_2O_7$/$GdCrO_3$ Composite for Hydrogen Evolution. *Dalton Trans.* **2011**, *40*, 12839−12845.
(39) Liu, Z.; Zhang, X.; Nishimoto, S.; Jin, M.; Tryk, D. A.; Murakami, T.; Fujishima, A. Highly Ordered $TiO_2$ Nanotube Arrays with Controllable Length for Photoelectrocatalytic Degradation of Phenol. *J. Phys. Chem. C* **2008**, *112*, 253−259.
(40) Xiong, X.; Zhang, X.; Xu, Y. Incorporative Effect of Pt and $Na_2CO_3$ on $TiO_2$- Photocatalyzed Degradation of Phenol in Water. *J. Phys. Chem. C* **2016**, *120*, 25689−25696.



DOI: 10.1021/acsomega.7b01250
*ACS Omega* 2017, 2, 9040−9056